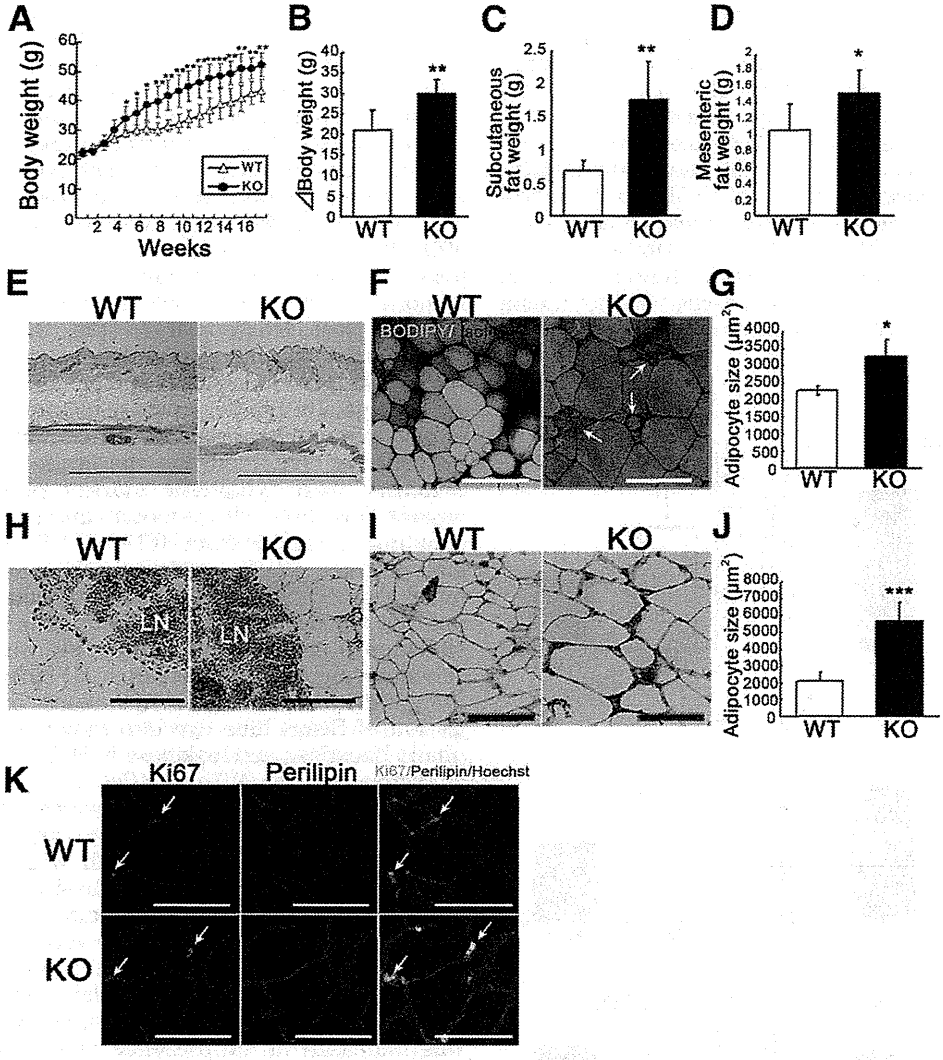

FIG. 1. Obesity in HFD-fed apelin KO mice. *A*: Body weight of HFD-fed apelin KO and WT mice (N = 7). Increased body weight (*B*), inguinal subcutaneous fat weight (*C*), and mesenteric fat weight (*D*) in apelin KO mice after 17 weeks of HFD. *E*: Hematoxylin and eosin staining showed a thickened subcutaneous fat layer in apelin KO mice. BODIPY (green) and Isolectin (red) staining revealed increased lipid droplet (green) size in subcutaneous adipocytes in apelin KO mice (*F*). Morphometric analysis of adipocyte size confirmed enlargement of adipocytes in apelin KO mice (*G*). Arrows show crown-like structures in obese fat pads. Hematoxylin and eosin staining of subcutaneous adipose tissue surrounding lymph nodes (LN) (*H*) and of mesenteric fat tissue (*I*). *J*: Morphometric analysis of mesenteric adipocyte size. Bars indicate 200 μm except in (*E*), which shows 1 mm. Date are expressed as mean values ± SD. *K*: Double immunofluorescence staining with Ki67 (green) and perilipin (red) in the mesenteric fat of WT and apelin KO mice after HFD. Arrows show proliferating adipocytes. ***$P < 0.001$, **$P < 0.01$, *$P < 0.05$.

adipocytes. Subcutaneous adipocytes in HFD-fed apelin KO mice were increased in size (Fig. 1*F*) and surrounded by endothelial cells, which appeared to form crown-like structures in obese fat pads, as described previously (14). Morphometric analysis confirmed that adipocytes were enlarged in the HFD-fed apelin KO mice (Fig. 1*G*). Sections of subcutaneous white adipose tissue around lymph nodes and sections of mesenteric fat tissue showed increased adipocyte size of apelin KO mice as compared with controls (Fig. 1*H–J*). Double immunofluorescence staining using antibodies against proliferation marker Ki67 and perilipin revealed no significant difference of proliferating adipocytes in mesenteric fat tissues between apelin KO mice and WT mice after HFD (Fig. 1*K*).

No major abnormality of food consumption or lipid metabolism in apelin KO mice. Because apelin/APJ signaling in the central nervous system contributes to body fluid homeostasis (18), we investigated the food consumption of HFD-fed apelin KO mice to determine if the obese phenotype of apelin KO mice was elicited by abnormality of hypothalamic function after HFD feeding. There was no significant difference in the amount of weekly food intake between apelin KO mice and their WT littermates (Fig. 2*A*). The plasma insulin level in obese apelin KO mice was slightly, but not significantly, decreased as compared with WT mice (Fig. 2*B*). However, the leptin concentration in apelin KO mice was significantly increased, whereas the adiponectin level was significantly decreased (Fig. 2*C*, *D*). We also measured the levels of circulating glucose, HDL cholesterol, triglycerides, and free fatty acids in the plasma of obese apelin KO mice and their WT counterparts but found no significant difference in any of these factors (Fig. 2*E–H*).

Abnormal lymphatic dysfunction and inflammation in skin of HFD-fed apelin KO mice. To examine infiltration of macrophages in the adipose tissue, we used immunohistochemical staining for CD11b. The results demonstrated an increase of infiltrating macrophages in the subcutaneous adipose layer of HFD-fed apelin KO mice, as compared with WT mice (Fig. 3*A*). Morphometric analysis confirmed an increased number of infiltrating macrophages in the subcutaneous adipose tissue of apelin KO mice ($P < 0.01$) (Fig. 3*B*). We have previously demonstrated that apelin promotes lymphatic function during inflammation (12). Therefore, to determine whether apelin depletion could lead to vascular abnormality in obese mice, we examined the expression of the APJ in lymphatic and blood vessels in vivo. Double immunofluorescence staining for the lymphatic marker podoplanin or the vascular marker meca-32 and APJ revealed weak APJ expression in cutaneous lymphatic vessels from mice fed RD, whereas HFD-fed mice showed increased expression of APJ in LECs (Fig. 3*C*). In contrast, APJ expression levels were similar in blood vessels of RD-fed and HFD-fed mice (Fig. 3*D*). Given these data, we speculated that disruption of apelin signaling resulted in abnormal structure of lymphatic or blood vessels and increased their leakiness. Lymphatic and blood vessels in dermis of HFD-fed apelin KO mice were clearly enlarged (Fig. 3*E*), and the diameter of lymphatic and blood vessels was increased compared with those in WT controls (Fig. 3*F*). In addition, to analyze the enlarged lymphatic structure in apelin KO mice, whole-mount immunofluorescence for claudin-5 also was performed. We confirmed that the large vessels stained for claudin-5 were lymphatic marker podoplanin-positive vessels (Fig. 3*G*). Whole-mount immunofluorescence for claudin-5 of ear skin from HFD-fed WT and apelin KO mice also revealed dilation of lymphatic vessels in apelin KO mice (Fig. 3*G*). Surprisingly, obese apelin-KO mice showed not only angiogenesis but also lymphatic hyperplasia in the subcutaneous fat layer, whereas this was not the case in subcutaneous adipose tissue of HFD-fed WT mice (Fig. 3*H*). Functional analyses by means of intradermal injection of Evans blue dye into mouse ears revealed lymphatic backflush and leakiness in HFD-fed apelin KO mice as compared with WT mice (Fig. 3*I*).

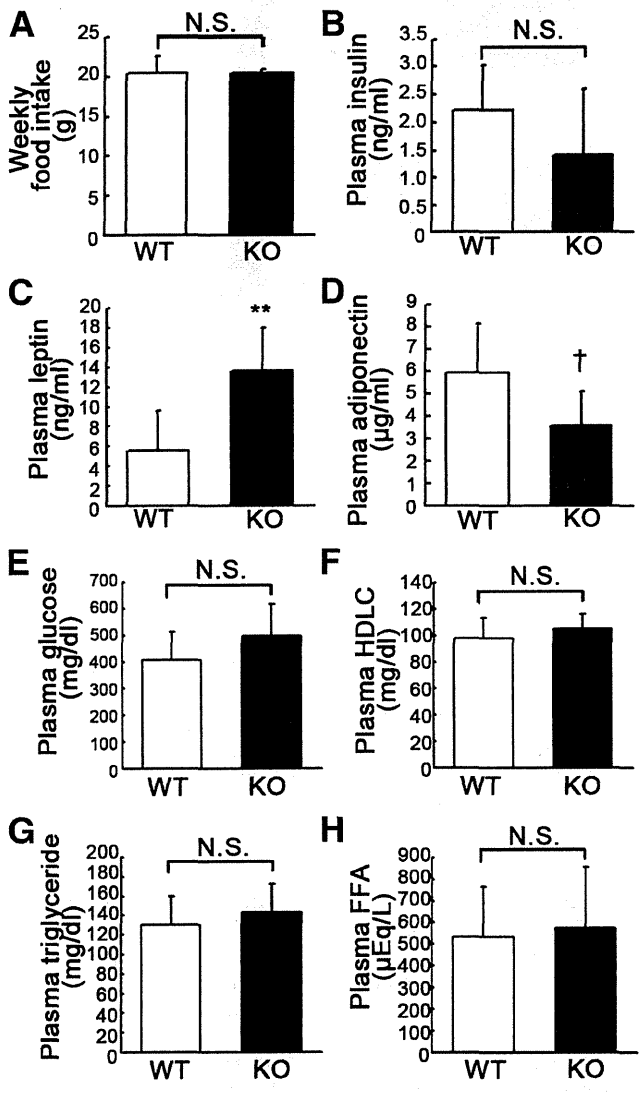

FIG. 2. No significant difference was found in food consumption or lipid metabolism between apelin KO and WT mice after HFD. *A*: Food intake was similar in apelin KO mice and WT littermates. *B*: Obese apelin KO mice had a lower plasma insulin level, but the difference was not significant. *C*: Serum leptin levels were approximately two times higher in apelin KO mice than in WT mice (**$P < 0.01$). *D*: Serum adiponectin levels tended to be lower in apelin KO mice, but the difference was not significant. There was no significant difference of plasma glucose (*E*), HDL cholesterol (HDLC; *F*), triglyceride (*G*), or free fatty acid (FFA; *H*) between apelin KO mice and WT mice. Data are expressed as mean values ± SD ($N = 7$; **$P < 0.01$, †$P < 0.1$). N.S., not significant.

Dietary fatty acids cause hyperpermeability of lymphatic and blood vessels and adipocyte hypertrophy. To understand the mechanism through which HFD-fed apelin KO mice developed significant obesity, we investigated in vitro the effects of dietary fatty acids on LECs. The 3T3-L1 preadipocytes were cocultured with confluent LECs on Transwell inserts in the presence of plasma from HFD-fed or RD-fed WT mice to mimic the lymphatic endothelial wall (Fig. 4*A*). Surprisingly, the amount of lipid droplets was increased in the presence of plasma from HFD-fed mice, whereas no major difference was found in the presence or absence of plasma from RD-fed mice (Fig. 4*B*, *C*). Because significant increases of oleic acid and stearic acid were found in plasma of HFD-fed mice (M. Takagi, unpublished observation), we speculated that the elevated fatty acids in plasma of HFD-fed mice would induce dysfunction of lymphatic and blood vessels via apelin depletion, thereby promoting obesity. Treatment of LECs with 20 and 100 μmol/L oleic acid resulted in hyperpermeability of LECs compared with untreated cells (Fig. 4*D*). Moreover, we confirmed that these dietary fatty acids promoted differentiation of human subcutaneous adipocytes (Fig. 4*E*). Preincubation with apelin-13 blocked the hyperpermeability of lymphatic and blood vessel endothelial cells induced by oleic acid (Fig. 4*F*, *G*). Moreover, whereas unstimulated endothelial cells were stained evenly with VE-cadherin at sites of cell–cell junctions, cells incubated with oleic acid displayed discontinuous staining with considerable gaps. Surprisingly, cells pretreated with apelin-13 before incubation with oleic acid retained the normal staining pattern of VE-cadherin (Fig. 4*H*). These data indicate that the oleic acid in HFD enhances the leakiness of lymphatic and vascular structures via disruption of VE-cadherin, and that leakage of dietary fatty acids from the vessels mediates adipocyte hypertrophy.

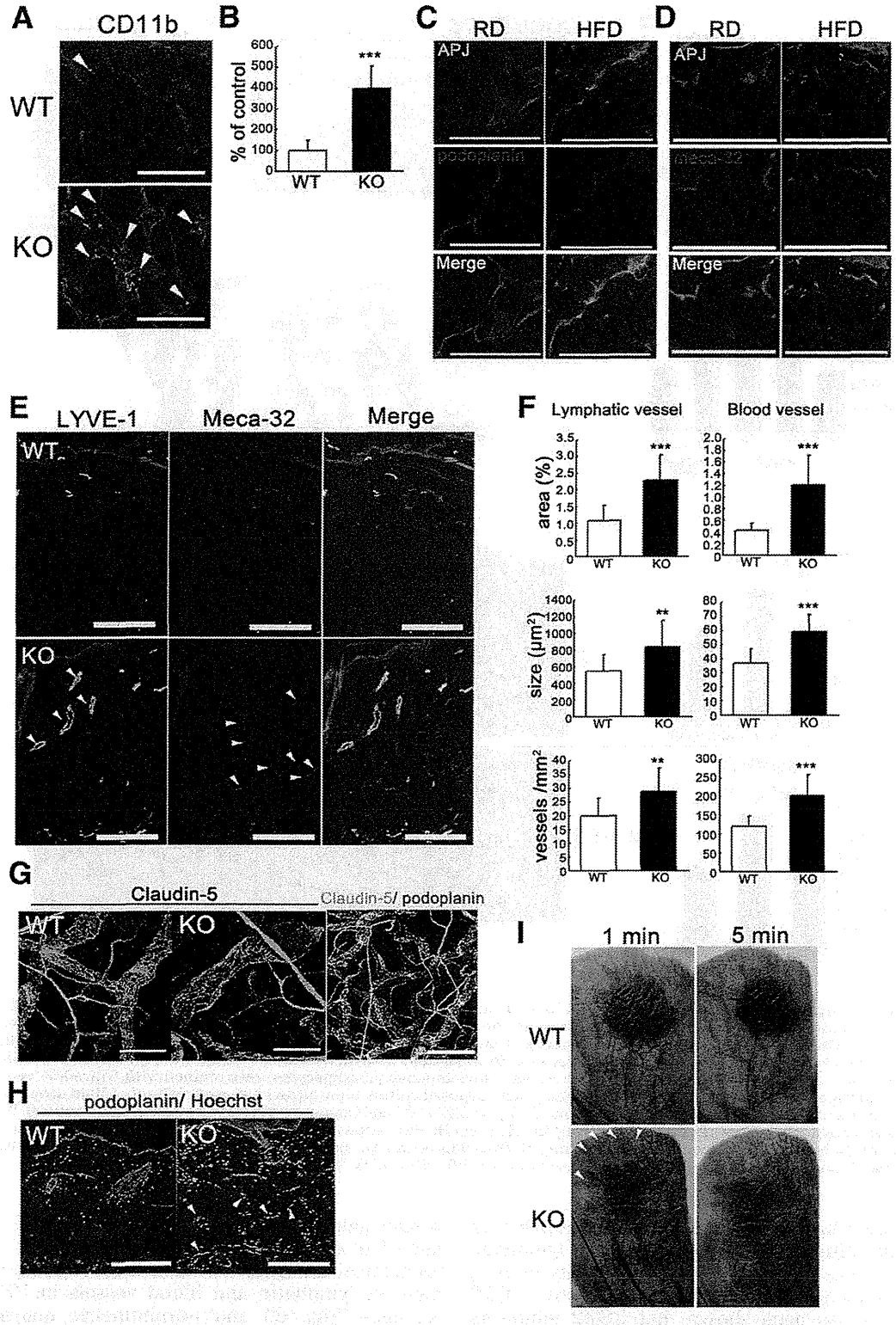

FIG. 3. Enhanced inflammation and vascular malformation in obese apelin KO mice. *A*: Increased CD11b$^+$ macrophages (green) in the subcutaneous adipose layer of skin from apelin KO mice. *B*: Morphometric analysis showed that the number of CD11b$^+$ macrophages was significantly increased in apelin KO mice. Double immunofluorescence staining for podoplanin (*C*, red) or meca-32 (*D*, red) and for APJ (green) revealed upregulated expression of APJ in lymphatics of skin of HFD-fed mice. *E*: Double immunofluorescence staining of skin for LYVE-1 (green) and meca-32 (red) revealed enlargement (arrowheads) and enhanced formation of LYVE-1$^+$ lymphatic vessels and meca-32$^+$ blood vessels in apelin KO mice. *F*: Computer-assisted morphometric analyses of lymphatic and blood vessels in skin. *G*: Immunofluorescence staining for claudin-5 in a whole-mount of ear skin. Lymphatic vessels in apelin KO mice were partly dilated compared with controls. Double immunofluorescence staining of claudin-5 (green) and podoplanin (red) confirmed that the nonuniform vessels were podoplanin-positive lymphatic vessels. *H*: Immunofluorescence analysis of mouse skin for podoplanin (red) revealed lymphatic hyperplasia in the adipose layer of apelin KO mice. *I*: Intradermal injection of Evans blue dye visualized enhanced leakiness of enlarged lymphatic vessels and lymphatic backflush (arrowheads) in apelin KO mice at 1 and 5 min after the injection. Scale bars indicate 200 μm except in (*G*), which indicates 100 μm. Data are expressed as mean values ± SD. $^{**}P < 0.01$, $^{***}P < 0.001$.

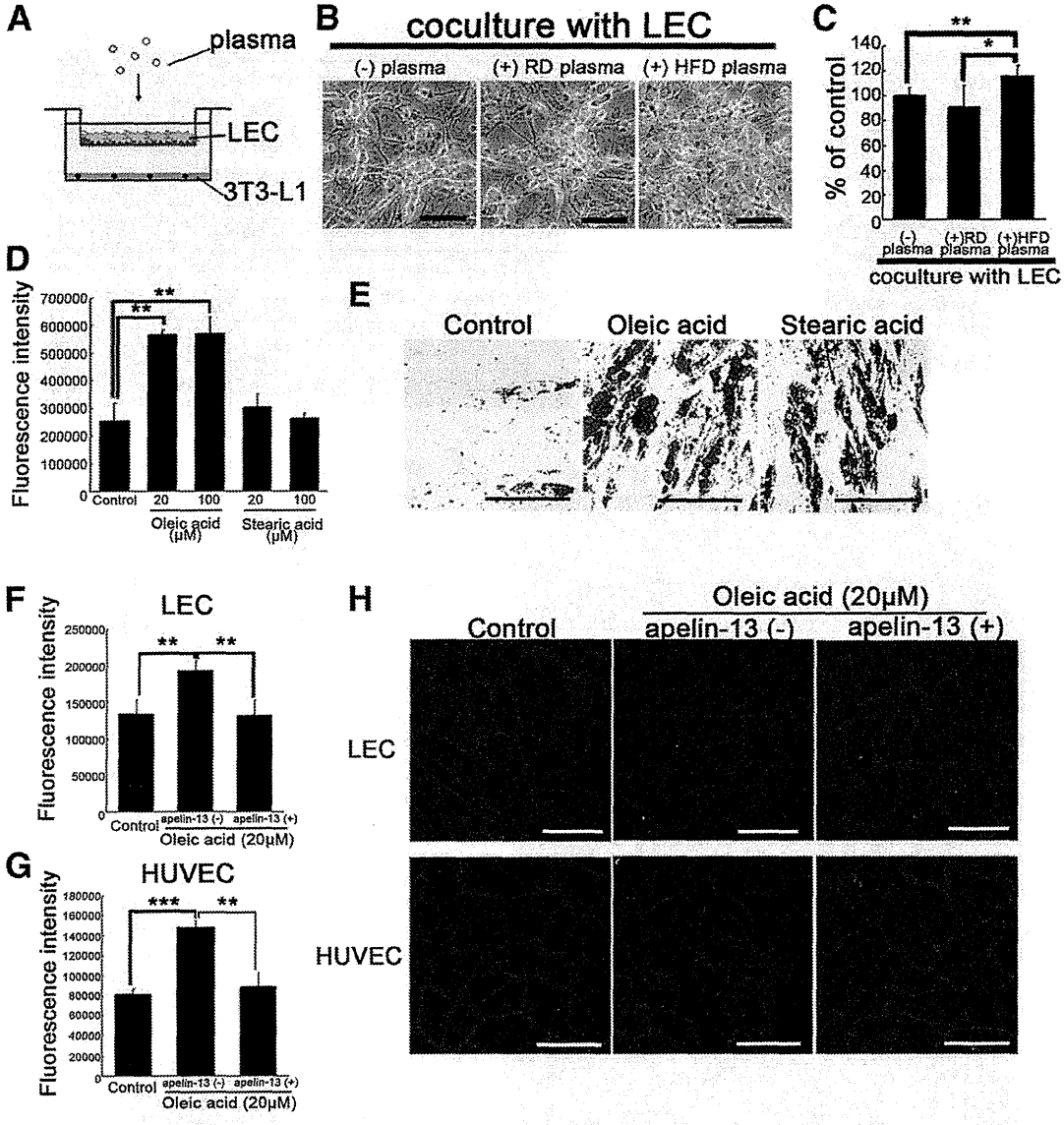

FIG. 4. Apelin inhibits vascular hyperpermeability induced by oleic acid, thereby blocking adipocyte differentiation. *A*: Schematic illustration of coculture study of LECs with 3T3-L1 preadipocytes in the presence or absence of plasma. Confluent LECs were inserted with or without plasma on day 2 after initiation of differentiation. *B*: 3T3-L1 preadipocytes were stained with Oil-red-O (red) on day 9 after initiation of differentiation. *C*: Quantitative evaluation of lipid droplets of 3T3-L1 preadipocytes. *D*: Treatment with oleic acid increased the fluorescence intensity of permeated FITC-dextran from LECs, as compared with the control. *E*: Human subcutaneous preadipocytes were stained with Oil-red-O (red) on day 9 after initiation of differentiation with oleic acid or stearic acid. Fatty acid–exposed culture showed an increased amount of lipid droplets compared with the control. The addition of apelin-13 blocked the hyperpermeability of LECs (*F*) and human umbilical vein endothelial cells (HUVECs; *G*) induced by oleic acid. *H*: Immunohistochemistry of VE-cadherin (red) in LECs and HUVEC, showing discontinuous staining of VE-cadherin after incubation with oleic acid. Apelin-13 blocked the discontinuity of staining of VE-cadherin and the gap formation induced by oleic acid. Scale bars indicate 200 μm (*E*) and 100 μm (*B* and *H*). Data are expressed as mean values ± SD. *$P < 0.05$, **$P < 0.01$, ***$P < 0.001$.

A selective COX2 inhibitor blocked the disruption of apelin/APJ signaling. To determine how the lymphatic and vascular systems affect HFD-induced obesity in vivo, we treated HFD-fed apelin KO mice with a selective COX2 inhibitor, CEL. It has been shown that COX2 inhibitors block angiogenesis and lymphangiogenesis during tumor growth (19). The CEL-treated, HFD-fed, apelin KO mice gained 30% less weight than HFD-fed apelin KO mice, and showed differences in subcutaneous and mesenteric fat accumulation (Fig. 5*A–D*). Hematoxylin and eosin staining of skin sections confirmed a decreased adipose layer in the CEL-treated apelin KO mice, with a decreased adipocyte diameter (Fig. 5*E, F*). However, no significant difference in weight gain or fat accumulation was found between WT mice fed with and without CEL (Fig. 5*A–D*). Immunohistochemical analyses revealed that CEL blocked enlargement of lymphatic and blood vessels in HFD-fed apelin KO mice (Fig. 5*G*), and morphometric analysis confirmed that the vessel size was decreased (Fig. 5*H*). Moreover, fat pads from CEL-treated, HFD-fed, apelin KO mice showed decreased $CD11b^+$ macrophages (Fig. 5*I*). CEL-treated, HFD-fed, apelin KO mice showed a decreased number of macrophages in subcutaneous adipose tissue (Fig. 5*J*). Further, CEL blocked the lymphatic and blood vascular hyperpermeability induced by oleic acid, like apelin-13 (Fig. 5*K*). In contrast, COX2 expression in LECs was

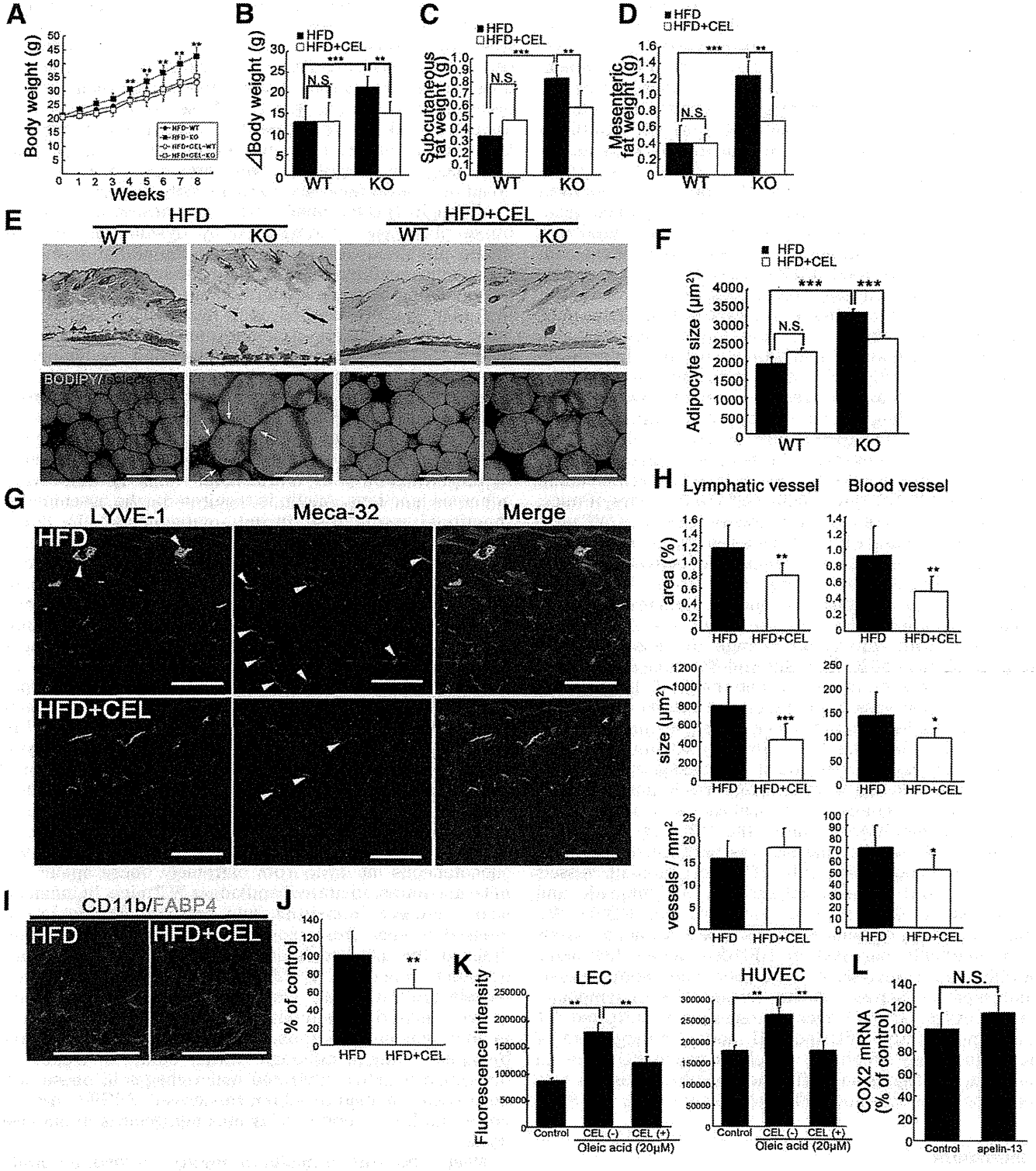

FIG. 5. Obesity induced by apelin depletion after HFD was blocked by orally administered selective COX2 inhibitor. A: Weight gain in WT and apelin KO mice maintained on HFD or HFD containing CEL (N = 3–7). The change of body weight (B) and tissue weight of inguinal subcutaneous (C) and mesenteric (D) fat after HFD or HFD with CEL. E: Histological analysis of skin and subcutaneous adipose tissue imaging using BODIPY (green) and Isolectin (red) showed that hypertrophic adipocytes (green) were reduced in CEL-treated HFD-fed apelin KO and WT mice. Arrows show crown-like structures in obese fat pads. F: Mean adipocyte size in CEL-treated, HFD-fed, apelin KO mice was smaller than in HFD-fed apelin KO mice. G: Immunohistochemical analyses for LYVE-1 (green) and meca-32 (red) revealed that enlargement of lymphatic and blood vessels (arrowheads) in the skin of HFD-fed apelin KO mice was inhibited by CEL. H: Morphometric analyses of lymphatic and blood vessels in CEL-treated, HFD-fed, apelin KO mice and HFD-fed apelin KO mice. I: Double immunofluorescence staining for CD11b (red) and FABP4 (green) showed that macrophage infiltration in the subcutaneous fat layer from HFD-fed apelin KO mice was blocked by CEL. J: The number of infiltrated macrophages was decreased in apelin KO mice fed HFD with CEL. K: Increased permeability in LECs and human umbilical vein endothelial cells (HUVECs) after the treatment with oleic acid was blocked by the addition of CEL. Bars indicate 1 mm (E, top) and 200 μm (E, bottom, G, and I). Data are expressed as mean values ± SD. L: COX2 expression after apelin treatment of LECs. $^{***}P < 0.001$, $^{**}P < 0.01$, and $^{*}P < 0.05$.

similar in controls and apelin-treated cells (Fig. 5*L*). Taken together, these results show that the selective COX2 inhibitor CEL ameliorated both inflammation and the dysfunction of lymphatic and blood vessels in HFD-fed apelin KO mice, resulting in the inhibition of HFD-induced obesity.

Resistance to obesity in apelin transgenic mice. To examine whether the stabilization of lymphatic and blood vessels by apelin inhibits the accumulation of fat tissue, we used apelin transgenic mice under the control of K14 (K14-apelin). Interestingly, HFD-fed K14-apelin mice showed significant inhibition of weight gain and decreased accumulation of subcutaneous adipose tissue as compared with HFD-fed WT mice, although there was no significant difference of weekly food intake between the two groups (Fig. 6*A*, *B*). The adipose layer of skin and the amount of subcutaneous adipose tissue in HFD-fed K14-apelin mice were decreased (Fig. 6*C*, *D*). Morphometric analysis also confirmed a decrease of lipid droplets within adipocytes in K14-apelin mice (Fig. 6*E*). Next, lymphatic function in the mesenteric fat was analyzed by injecting dye into the stomach, revealing the inhibition of lymphatic hyperpermeability in K14-apelin mice as compared with WT mice (Fig. 6*F*). To evaluate the structural change of lymphatic and blood vessels, we performed whole-mount staining for LYVE-1 (green)/meca-32 (red) in ears of mice. Interestingly, both blood and lymphatic vessels of WT mice were enlarged after HFD, whereas the diameters of blood and lymphatic vessels were comparable between RD- and HFD-fed K14-apelin mice (Fig. 6*G*). These results are consistent with the idea that apelin regulates the accumulation of adipose tissue by promoting vessel integrity.

Structural and functional change of vessels in the adipose tissues of K14-apelin and KO mice after HFD. Miles assay was performed to determine of the effect of apelin on blood vessels in epididymal fat. We found that leakiness was inhibited in K14-apelin mice and enhanced in apelin KO mice after HFD (Fig. 7*A*). Quantitative analysis showed that HFD enhanced dye leakage in WT mice, whereas the increase of dye leakage was inhibited in K14-apelin mice. In contrast, dye leakage was strongly enhanced in apelin KO mice after HFD (Fig. 7*B*).

Immnofluorescence analysis was performed with antibodies for blood vessels (Fig. 7*C*) and lymphatic vessels (Fig. 7*E*). HFD induced enlargement of lymphatic and blood vessels of WT mice as compared with RD-fed WT mice. Moreover, lymphatic vessels as well as blood vessels were markedly enlarged in HFD-fed apelin KO mice. Morphometric analysis of lymphatic and blood vessels confirmed an increase in the average size of lymphatic vessels of HFD-fed WT mice as compared with RD-fed WT mice. Importantly, HFD induced marked enlargement of both blood and lymphatic vessels in apelin KO mice. In contrast, no significant difference of blood vessels was found between RD- and HFD-fed WT mice (Fig. 7*D*, *F*).

DISCUSSION

Our results indicate that apelin/APJ signaling plays a crucial role in the control of fat accumulation by enhancing the integrity of lymphatic and blood vessels. It is well-established that fat intake is associated with the growth of adipose tissue vasculature. This, in turn, suggests that inhibition of angiogenesis in adipose tissue could be an approach to treat obesity, but this idea is controversial because of the physiological importance of angiogenesis. It was reported that partial blockade of the VEGFR pathway had no effect on diet-induced obesity (5). Additionally, recent reports indicated that blocking the VEGFR-3 pathway in skin resulted in an increase of subcutaneous adipose tissue (20), and that Prox1 heterozygous mice showed obesity and abnormal lymphatic function, particularly at the mesentery and thoracic duct (7). These results suggest that there is a link between lymphatic function and adipose tissue accumulation. Here, we propose that a strategy of enhancing the integrity of lymphatic and blood vessels could be a novel approach to antiobesity therapy.

Although HFD-fed apelin KO mice showed a markedly obese phenotype accompanied by dysfunction of lymphatic and blood vessels, it was also found that there was no significant difference of either vessel function or fat accumulation between apelin KO and WT mice fed a normal diet. These results led us to hypothesize that dietary fatty acids accelerate vascular damage via apelin depletion, because fatty acids are absorbed by lymphatic vessels and transported to peripheral tissues by blood vessels. Our in vitro study demonstrated that plasma from HFD-fed mice increased the amount of lipid droplets of 3T3-L1 preadipocytes by disrupting lymphatic integrity and that oleic acid, a dietary fatty acid, directly mediates hyperpermeability of endothelial cells by disrupting adherens junctions. Apelin is required for the assembly of functional vasculature during angiogenesis (11). Interestingly, apelin inhibited oleic acid–induced vascular hyperpermeability by modulating VE-cadherin in vitro. Taken together, these results indicate that HFD-fed apelin KO mice develop abnormal vascular leakiness and structure as a result of the synergistic effects of apelin depletion and increase of oleic acid. Importantly, lymphatic backflush and abnormal leakiness were found in the ear skin of HFD-fed apelin KO mice. In vitro, lymphatic permeability was induced in the presence of fatty acids, whereas apelin attenuated the fatty acid–induced hyperpermeability. Because leakiness and structural abnormalities of skin lymphatic vessels are seen in apolipoprotein E–deficient mice (21), these results suggest that abnormal transportation and lymphatic absorbance of fatty acids from peripheral tissues like skin could be involved in the development of obesity. Moreover, lymphatic hyperplasia was found in the subcutaneous fat layer from extremely obese apelin KO mice in contrast to normal and obese WT mice. In inflamed skin, increased interstitial fluid pressure caused by increased leakage from blood vessels may increase fluid drainage through lymphatic vessels, but this may impair lymphatic function (22). Thus, an increase of lymphatic vessels could facilitate lymphatic drainage and resolution of the related inflammation (23,24). Therefore lymphangiogenesis in adipose tissue could be a significant therapeutic target, although further study is needed to determine whether infiltrated macrophages in obese adipose tissue or mature adipocyte-derived VEGF-C are involved in the promotion of lymphangiogenesis in adipose tissue.

What is the role of apelin in obesity? In vivo, an orally administered COX2 inhibitor rescued apelin KO mice from HFD-induced obesity. A COX2 inhibitor directly affects vascular function, suppressing angiogenesis and lymphangiogenesis associated with tumor growth (19). The COX2 inhibitor, CEL, blocked angiogenesis and blood/lymphatic vessel enlargement in HFD-fed apelin KO mice. In vitro, we found that CEL treatment blocked oleic acid–induced hyperpermeability of lymphatic and blood vessel endothelial cells. Taken together with the fact that several

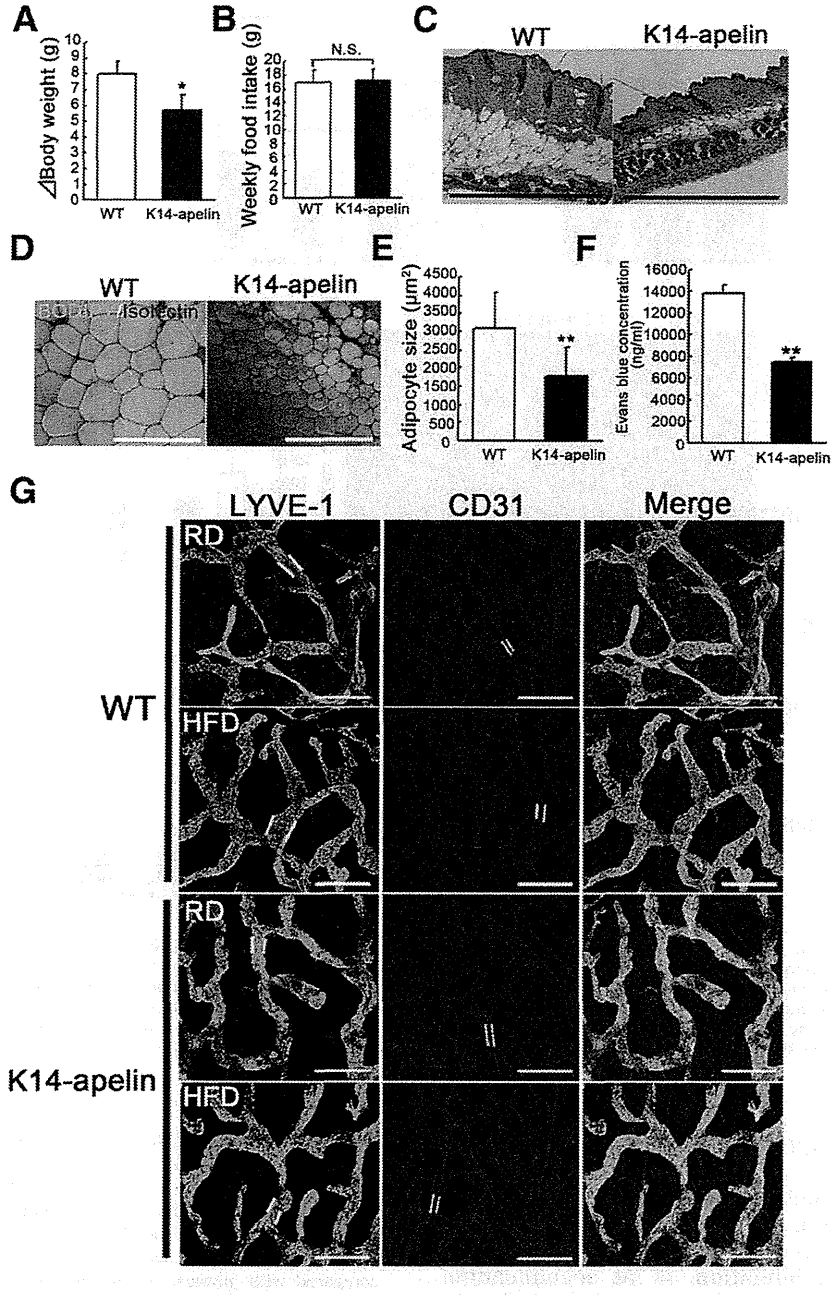

FIG. 6. Resistance to obesity in K14-apelin mice. *A*: Change in body weight of HFD-fed K14-apelin and WT mice (N = 4–7). *B*: Average weekly food intake of each genotype. *C*: Hematoxylin and eosin staining of skin sections from HFD-fed, K14-apelin, and WT mice. A reduced subcutaneous adipose layer was found in K14-apelin mice. *D*: BODIPY (green) and Isolectin (red) staining revealed decreased size of subcutaneous adipocytes (green) in K14-apelin mice after HFD feeding. *E*: Morphometric analysis of adipocyte size confirmed that adipocytes were smaller in HFD-fed K14-apelin mice. Data are expressed as mean values ± SD. *F*: Inhibition of lymphatic dye leakage in mesenteric fat of K14-apelin mice after HFD. *G*: Whole-mount staining of mouse ears using antibodies against LYVE-1 (green) and CD31 (red) revealed that HFD induced enlargement of both lymphatic and blood vessels, whereas no significant difference was found between RD- and HFD-fed K14-apelin mice. Two parallel yellow lines as indicated in (*G*) show vascular size. Bars indicate 1 mm (*C*) and 200 μm (*D*, *G*). $^{**}P < 0.01$, $^{*}P < 0.05$.

dietary fatty acids increased the expression level of transcription factors associated with adipocyte differentiation, including peroxisome proliferator–activated receptors (25), leakage of dietary fatty acids, possibly from hyperpermeable vessels, could accelerate adipocyte differentiation. In addition, a selective COX2 inhibitor did not affect fat accumulation of WT mice, although the number of blood vessels in skin was decreased. Taking into account the fact that no significant change of COX2 expression was found after apelin treatment in endothelial cells, this is consistent with the idea that a selective COX2 inhibitor could directly block the development of vascular hyperpermeability in HFD-fed apelin KO mice, leading to inhibition of obesity. The increased leakage of fatty acids attributable to the disruption of lymphatic and vascular function could trigger adipocyte hypertrophy. Recently, it has been reported that overexpression of COX2 in skin increased energy expenditure via recruitment of brown

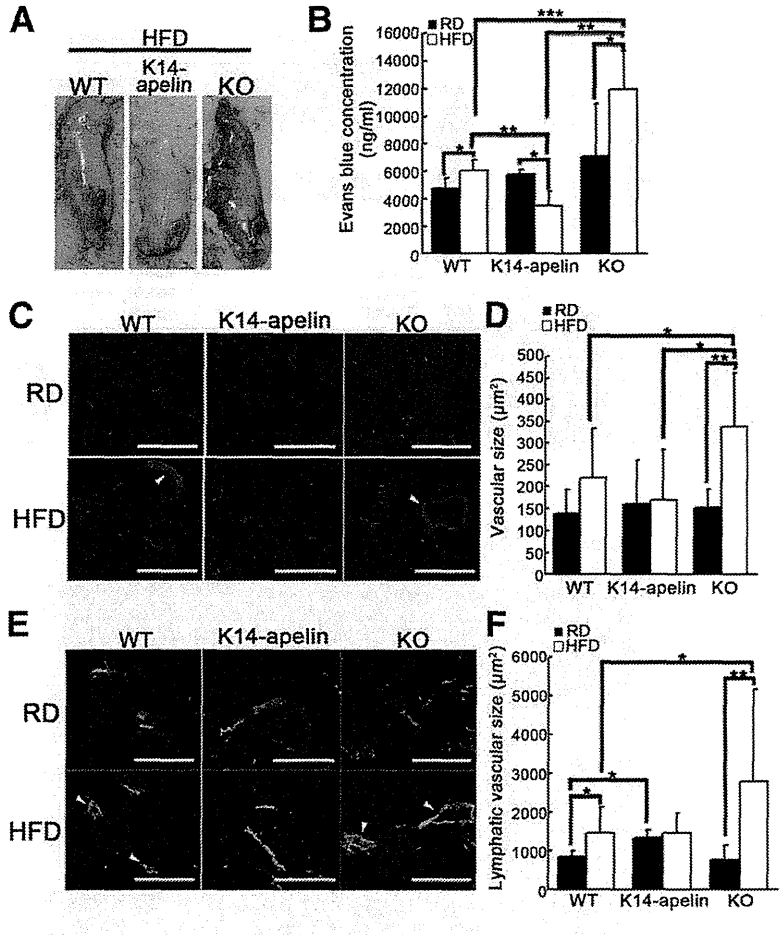

FIG. 7. Structural and functional changes of vessels in the adipose tissues of K14-apelin and apelin KO mice after HFD. *A*: Miles assay revealed increased Evans blue leakage in epididymal fat of apelin KO mice and decreased leakage in that of K14-apelin mice as compared with WT mice after feeding of HFD. *B*: Quantitative analysis of dye leakage in the epididymal fat showed that HFD enhanced dye leakage in WT and apelin KO mice, whereas dye leakage was blocked in K14-apelin mice. Immunofluorescence analysis using antibodies against meca-32 (*C*) and LYVE-1 (*E*) in mesenteric fat. Arrowheads show enlarged blood vessels (*C*) and lymphatic vessels (*E*). Quantitative analysis of blood vessels (*D*) and lymphatic vessels (*F*) in mesenteric fat of WT, K14-apelin, and apelin KO mice. Bars indicate 200 μm. **$P < 0.01$, *$P < 0.05$.

adipocytes (26). Therefore, further investigation of the role of apelin in COX2-overexpressing brown adipose tissue is needed.

In conclusion, our results indicate that apelin/APJ signaling promotes lymphatic and blood vessel integrity and blocks the increase of permeability induced by dietary fatty acids, resulting in inhibition of fat accumulation. Apelin might be a novel target for prevention of obesity and obesity-related diseases via enhancement of vascular integrity.

ACKNOWLEDGMENTS

No potential conflicts of interest relevant to this article were reported.

M.S. and K.K. designed and performed research, analyzed data, and wrote the paper. H.K., M.T., and F.M. performed research and analyzed data. N.T. designed research and wrote the paper. K.K. is the guarantor of this work and, as such, had full access to all the data and takes full responsibility for the integrity of data and accuracy of data analysis.

The authors thank Fumika Miyohashi and Kyo Suin (Shiseido Innovative Science Research Center, Yokohama, Japan) for their technical assistance.

REFERENCES

1. Rosen ED, Spiegelman BM. Adipocytes as regulators of energy balance and glucose homeostasis. Nature 2006;444:847–853
2. Oliver G, Detmar M. The rediscovery of the lymphatic system: old and new insights into the development and biological function of the lymphatic vasculature. Genes Dev 2002;16:773–783
3. Hu FB, Willett WC, Li T, Stampfer MJ, Colditz GA, Manson JE. Adiposity as compared with physical activity in predicting mortality among women. N Engl J Med 2004;351:2694–2703
4. Crandall DL, Hausman GJ, Kral JG. A review of the microcirculation of adipose tissue: anatomic, metabolic, and angiogenic perspectives. Microcirculation 1997;4:211–232
5. Cao Y. Adipose tissue angiogenesis as a therapeutic target for obesity and metabolic diseases. Nat Rev Drug Discov 2010;9:107–115
6. Karkkainen MJ, Saaristo A, Jussila L, et al. A model for gene therapy of human hereditary lymphedema. Proc Natl Acad Sci USA 2001;98:12677–12682
7. Harvey NL, Srinivasan RS, Dillard ME, et al. Lymphatic vascular defects promoted by Prox1 haploinsufficiency cause adult-onset obesity. Nat Genet 2005;37:1072–1081
8. Tatemoto K, Hosoya M, Habata Y, et al. Isolation and characterization of a novel endogenous peptide ligand for the human APJ receptor. Biochem Biophys Res Commun 1998;251:471–476
9. Chen MM, Ashley EA, Deng DX, et al. Novel role for the potent endogenous inotrope apelin in human cardiac dysfunction. Circulation 2003;108:1432–1439
10. Kidoya H, Ueno M, Yamada Y, et al. Spatial and temporal role of the apelin/APJ system in the caliber size regulation of blood vessels during angiogenesis. EMBO J 2008;27:522–534

11. Kidoya H, Naito H, Takakura N. Apelin induces enlarged and nonleaky blood vessels for functional recovery from ischemia. Blood 2010;115:3166–3174
12. Sawane M, Kidoya H, Muramatsu F, Takakura N, Kajiya K. Apelin attenuates UVB-induced edema and inflammation by promoting vessel function. Am J Pathol 2011;179:2691–2697
13. Kajiya K, Hirakawa S, Ma B, Drinnenberg I, Detmar M. Hepatocyte growth factor promotes lymphatic vessel formation and function. EMBO J 2005;24:2885–2895
14. Nishimura S, Manabe I, Nagasaki M, et al. In vivo imaging in mice reveals local cell dynamics and inflammation in obese adipose tissue. J Clin Invest 2008;118:710–721
15. Hirakawa S, Hong YK, Harvey N, et al. Identification of vascular lineage-specific genes by transcriptional profiling of isolated blood vascular and lymphatic endothelial cells. Am J Pathol 2003;162:575–586
16. Yamamoto Y, Yoshimasa Y, Koh M, et al. Constitutively active mitogen-activated protein kinase kinase increases GLUT1 expression and recruits both GLUT1 and GLUT4 at the cell surface in 3T3-L1 adipocytes. Diabetes 2000;49:332–339
17. Calkhoven CF, Müller C, Leutz A. Translational control of C/EBPalpha and C/EBPbeta isoform expression. Genes Dev 2000;14:1920–1932
18. Reaux A, De Mota N, Skultetyova I, et al. Physiological role of a novel neuropeptide, apelin, and its receptor in the rat brain. J Neurochem 2001;77:1085–1096
19. Iwata C, Kano MR, Komuro A, et al. Inhibition of cyclooxygenase-2 suppresses lymph node metastasis via reduction of lymphangiogenesis. Cancer Res 2007;67:10181–10189
20. Mäkinen T, Jussila L, Veikkola T, et al. Inhibition of lymphangiogenesis with resulting lymphedema in transgenic mice expressing soluble VEGF receptor-3. Nat Med 2001;7:199–205
21. Lim HY, Rutkowski JM, Helft J, et al. Hypercholesterolemic mice exhibit lymphatic vessel dysfunction and degeneration. Am J Pathol 2009;175:1328–1337
22. Kajiya K, Hirakawa S, Detmar M. Vascular endothelial growth factor-A mediates ultraviolet B-induced impairment of lymphatic vessel function. Am J Pathol 2006;169:1496–1503
23. Huggenberger R, Ullmann S, Proulx ST, Pytowski B, Alitalo K, Detmar M. Stimulation of lymphangiogenesis via VEGFR-3 inhibits chronic skin inflammation. J Exp Med 2010;207:2255–2269
24. Kajiya K, Sawane M, Huggenberger R, Detmar M. Activation of the VEGFR-3 pathway by VEGF-C attenuates UVB-induced edema formation and skin inflammation by promoting lymphangiogenesis. J Invest Dermatol 2009;129:1292–1298
25. Madsen L, Petersen RK, Kristiansen K. Regulation of adipocyte differentiation and function by polyunsaturated fatty acids. Biochim Biophys Acta 2005;1740:266–286
26. Vegiopoulos A, Müller-Decker K, Strzoda D, et al. Cyclooxygenase-2 controls energy homeostasis in mice by de novo recruitment of brown adipocytes. Science 2010;328:1158–1161

THE JOURNAL OF BIOLOGICAL CHEMISTRY VOL. 288, NO. 18, pp. 12469–12477, May 3, 2013

Ligand-independent Tie2 Dimers Mediate Kinase Activity Stimulated by High Dose Angiopoietin-1*[S]

Received for publication, November 5, 2012, and in revised form, February 19, 2013 Published, JBC Papers in Press, March 15, 2013, DOI 10.1074/jbc.M112.433979

Daishi Yamakawa[‡], Hiroyasu Kidoya[‡], Susumu Sakimoto[‡], Weizhen Jia[‡], Hisamichi Naito[‡], and Nobuyuki Takakura[‡§1]

From the [‡]Department of Signal Transduction, Research Institute for Microbial Diseases, Osaka University, 3-1 Yamada-oka, Suita-shi, Osaka 565-0871, Japan and [§]Japan Science and Technology Agency (JST), Sanbancho, Chiyoda-ku, Tokyo 102-0075, Japan

Background: Tie2 is essential for angiogenesis and vascular stabilization.
Results: Tie2, but not Tie1, forms ligand-independent dimers on the cell surface.
Conclusion: The inactive monomer mutant Tie2YIA/LAS decreases Ang1/Tie2 signaling.
Significance: The Tie2 ligand-independent dimer induces strong phosphorylation upon high dose Ang1 binding.

Tie2 is a receptor tyrosine kinase expressed on vascular endothelial cells (ECs). It has dual roles in promoting angiogenesis and stabilizing blood vessels, and it has been suggested that Tie2 forms dimers and/or oligomers in the absence of angiopoietin-1 (Ang1); however, the mechanism of ligand-independent dimerization of Tie2 and its biological significance have not been clarified. Using a bimolecular fluorescence complementation assay and a kinase-inactive Tie2 mutant, we show here that ligand-independent Tie2 dimerization is induced without Tie2 phosphorylation. Moreover, based on the fact that Tie1 never forms heterodimers with Tie2 in the absence of Ang1 despite having high amino acid sequence homology with Tie2, we searched for ligand-independent dimerization domains of Tie2 by reference to the difference with Tie1. We found that the YIA sequence of the intracellular domain of Tie2 corresponding to the LAS sequence in Tie1 is essential for this dimerization. When the YIA sequence was replaced by LAS in Tie2 (Tie2YIA/LAS), ligand-independent dimer was not formed in the absence of Ang1. When activation of Tie2YIA/LAS was induced by a high dose of Ang1, phosphorylation of Tie2 was limited compared with wild-type Tie2, resulting in retardation of activation of Erk downstream of Tie2. Therefore, these data suggest that ligand-independent dimerization of Tie2 is essential for a strong response upon stimulation with high dose Ang1.

The functions of angiopoietin-1 (Ang1),[2] a ligand for receptor tyrosine kinase Tie2 expressed on endothelial cells (ECs), in both EC-to-EC and EC-to-mural cell adhesion are well established (1–4). Although Ang1-Tie2 signaling is involved in promoting maturation and quiescence of blood vessels mainly regulated by Akt signal transduction via the p85 subunit of PI3K, Tie2 also has proangiogenic activity mediated by MAPK signaling (5–7). Because Tie2 possesses both anti-angiogenic as well as proangiogenic properties, it is important to investigate how Tie2 activation is altered during angiogenesis. The Tie receptor family consists of Tie2 and Tie1 (8–10). Recent studies show that Ang1 activates Tie1 indirectly by interactions with Tie2 (11). When Tie1 expression is silenced, Tie2 signaling especially via the MAPK pathway is enhanced; accordingly, Tie1-deficient mice show hyperproliferative vascular formation and vascular abnormalities (12, 13). This suggests that Tie1 may negatively regulate angiogenic signaling by Tie2.

Tie2 is composed of an extracellular domain, one transmembrane domain, and an intracellular tyrosine kinase domain split into two by a non-kinase sequence. Tie1 has high amino acid sequence homology with Tie2 (76 and 33% identity in intracellular and extracellular domains, respectively). Based on the isolation of Tie2 ligands and analysis of signal transduction through Tie2, it is widely accepted that Ang1 activates Tie2, but Ang2 binding inhibits its signaling. Thus, with certain exceptions Ang2 acts as an Ang1 antagonist (4, 13–18).

It is known that Tie2 is present on the EC surface in the form of dimers and higher order oligomers, as established by electron microscopy (19). It has been reported that EGF receptor, erythropoietin receptor, and TNF receptor also dimerize in a ligand-independent manner (20–25). Ligand-independent dimerization of EGF receptor does not lead to tyrosine phosphorylation of EGF receptor. It has been suggested that a conformational change of the EGF receptor induces kinase activity on ligand binding. Therefore, ligand-independent dimers may mediate rapid signal transduction responses. Although Tie2 also forms ligand-independent dimers, the importance of this has not yet been determined.

In the present study, we established a system for visualization of Tie2 dimers using bimolecular fluorescence complementation (BiFC) assays in living cells (26). Using this system, we sought Ang1-independent Tie2-Tie2 dimerization domains. We generated a Tie2 mutant that does not form dimers in the absence of Ang1. We investigated the biological significance of ligand-independent Tie2 dimerization using this mutant.

* This work was supported in part by a grant from the Ministry of Education, Science, Sports, and Culture of Japan.
[S] This article contains supplemental Table S1 and Figs. S1–S6.
[1] To whom correspondence should be addressed: Dept. of Signal Transduction, Research Institute for Microbial Diseases, Osaka University, 3-1 Yamada-oka, Suita-shi, Osaka 565-0871, Japan. Tel.: 81-6879-8316; Fax: 81-6879-8314; E-mail: ntakaku@biken.osaka-u.ac.jp.
[2] The abbreviations used are: Ang1, angiopoietin-1; EC, endothelial cell; BiFC, bimolecular fluorescence complementation; Ab, antibody.

EXPERIMENTAL PROCEDURES

Reagents and Antibodies—Recombinant human Angl was purchased from R&D Systems. In Western blot analysis, mouse anti-phosphotyrosine (4G10) and anti-Tie2 (Ab33) antibodies (Abs) (Upstate), anti-HA.11 mAb (COVANCE), anti-c-Myc (9E10) and Tiel (C-18) mAbs (Santa Cruz Biotechnology, Inc.), anti-HA-tag rabbit serum (Medical & Biological Laboratories Co., Ltd.), p44/42, phospho-p44/42 (Thr^{202}/Tyr^{204}), phospho-Tie2 (Tyr^{992}) Abs (Cell Signaling Technology, Inc.) and mouse anti-HA (12CA5) mAb (Roche Diagnostics) were used as the first Abs. Anti-phospho-Tie2 (Tyr^{992}) and anti-phosphotyrosine Abs were diluted 1:500, and others were diluted 1:1000. HRP-conjugated anti-rabbit and anti-mouse IgG (Jackson ImmunoResearch Laboratories) was used as the secondary antibody (dilution: 1:1000). For the immunofluorescence analysis, HA and Myc were used as the first Abs (dilution, 1:100). Alexa Fluor 546-conjugated goat anti-rabbit Igs and Alexa Fluor 647-conjugated goat anti-mouse Igs were used as the secondary Abs (Invitrogen) (dilution, 1:200).

Plasmid Construction—Mouse Tie2 and Tiel were fused to sequences encoding full-length Venus and Venus residues 1–173 amino acids (VN) or 155–238 amino acids (VC). The coding regions were connected with linker sequences encoding RSAIT (Arg-Ser-Ala-Ile-Thr). RSAIT is a non-adhesion sequence (26). HA or Myc epitopes were inserted as tags between linker and fluorescent genes. Genes were inserted at the multicloning site in pEGFPN1 vector or pMRX virus vector. Basing the work on the pE-Tie2-linker-Myc-Venus, pE-Tie2-linker-HA-VN and pE-Tie2-linker-Myc-VC, we cut between the BamHI and MluI sites and the Tie2 mutant (Tie2K854R, Tie2R848W) was created. Tie2 kinase-dead (Tie2K854R) or Tie2 constitutive-active (Tie2R848W) mutants were amplified from wild-type Tie2 using Tie2K854R-N, -C primers or Tie2R848W-N, -C primers, respectively (supplemental Table S1).

For the generation of Tiel*, the signal sequence of Tie2 was amplified from the Tie2 plasmid using oligonucleotide primers (forward primer, 5′-GTA GGC GTG TAC GGT GGG AGG TCT-3′ and reverse primer, 5′-GTT AAG TCA ACA GAG CCT TCT ACT ACT CC-3′) and 5′-Tiel core sequence excluding signal sequence was amplified from Tiel using oligonucleotide primers (forward primer, 5′-GGA GTA GTA GAA GGC TCT GTT GAC TTA AC-3′ and reverse primer, 5′-CCA CTT CTG AGC TTC ACA GCC TCG CAC GAT-3′). These two products were amplified with the forward primer for Tie2 and the reverse primer for Tiel. This PCR product was placed into EcoRI and AgeI sites of the Tiel plasmid. For the generation of Tie2/Tiel chimeric plasmids, mutagenesis was performed on Tie2 and Tiel plasmids as templates by using specific primer sets (supplemental Table S1). For generation of 1–3 amino acid mutants of each Tie2 plasmid, mutagenesis was performed using specific primers (supplemental Table S1).

Retroviral Infection—Plat-E cells were transfected with pMRX-Tie2-linker-Myc-Venus, pMRX-Tie2YIA/LAS-linker-Myc-Venus, pMRX-Tie2-linker-HA-VN173 and pMRX-Tie2-linker-Myc-VC155, pMRX-Tie2YIA/LAS-linker-HA-VN173 and pMRX-Tie2YIA/LAS-linker-Myc-VC155 vectors as indicated in each experiment (1.0 μg each) using Lipofectamine 2000 (Invitrogen) and then incubated for 24 h at 37 °C after which the medium was changed. After 12 (36 h from transfection) and 24 h (48 h from transfection), conditioned medium was harvested, sterilized by filtration, and used to infect NIH3T3 cells. 8 μg/ml polybrene was added for enhancement of infection. Stable cell lines were selected by culture in medium containing puromycin (5 μg/ml) or blasticidin (10 μg/ml) (27, 28).

Cell Culture—HEK293T and NIH3T3 lines were grown in DMEM supplemented with 10% FBS. Platinum-E cells (Plat-E; packaging cells) and stable cell lines transfected by pMRX virus vector were cultured in 10% FBS containing DMEM.

Transfection and Bimolecular Fluorescence Complementation Analysis—To carry out BiFC in living cells, cells were co-transfected with the expression vectors indicated in each experiment (1.0 μg each) using Lipofectamine 2000. The fluorescence emissions were acquired in living cells 22–48 h after transfection using a fluorescence microscope with a cooled CCD camera, or by flow cytometry. Protein expression levels were assessed by Western blotting.

Cell Lysis, Immunoprecipitation, SDS-PAGE, and Western Blotting—Cells were washed with ice-cold PBS and lysed with radioimmune precipitation assay lysis buffer (50 mM Tris-HCl, pH 7.5, 150 mM NaCl, 1% Nonidet P-40, 0.5% sodium deoxycholate, 0.1% SDS). The cells were incubated on ice for 10 min followed by centrifugation at 15,000 rpm for 5 min at 4 °C. Cells were immunoprecipitated from the supernatant using 1–2 μg of anti-Myc Ab that had been precoupled to 20 μl of protein A-Sepharose 4 Fast Flow (GE Healthcare).

Proteins electrophoretically separated using 7.5% SDS gels were transferred to nylon membranes (Amersham Biosciences) by a wet blotting procedure (140 V, 200 mA, 120 min). The membrane was blocked with 5% skim milk/TBST for 60 min, subsequently incubated with the Abs as indicated in the figures and processed for chemiluminescence detection with ECL solution. Densitometry was performed with NIH ImageJ software (version 1.43u).

FACS Analysis—BiFC was analyzed by flow cytometry. After fluorescence complementation, cells were washed with PBS and resuspended in PBS. FACS analysis was performed with a FACSCalibur (BD Biosciences) using the 488 nm laser for excitation and a 515–545 nm band pass filter for detection. For quantitative evaluation of BiFC fluorescence, we used % Gated (fluorescent cells) × *X* Geo Mean (average of fluorescent intensity) as arbitrary fluorescence units.

Confocal Laser Scanning Microscopy—Transfected cells on 0.1% gelatin-coated glass dishes (Sigma Aldrich) were rinsed, fixed for 10 min in 4% paraformaldehyde-PBS (pH 7.5), and washed with PBS. Subsequently, the cells were permeabilized with 0.1% Triton X-100 for 10 min. After washing with PBS, cells were blocked with PBS containing 5% normal goat serum and 1% BSA for 30 min and immunostained with first Ab (1:100) for 1 h. Protein reacting with Ab was visualized with secondary Abs (1:200). HA or Myc epitopes were inserted as tags between Tie2 or Tie2YIA/LAS and the BiFC tag (VN or VC). HA-VN fused with Tie2 or Tie2YIA/LAS was stained by rabbit anti-HA Ab (Medical & Biological Laboratories Co., Ltd.) and Alexa Fluor 546 (red)-conjugated anti-rabbit Igs. Myc-VC fused with Tie2 or Tie2YIA/LAS was stained with

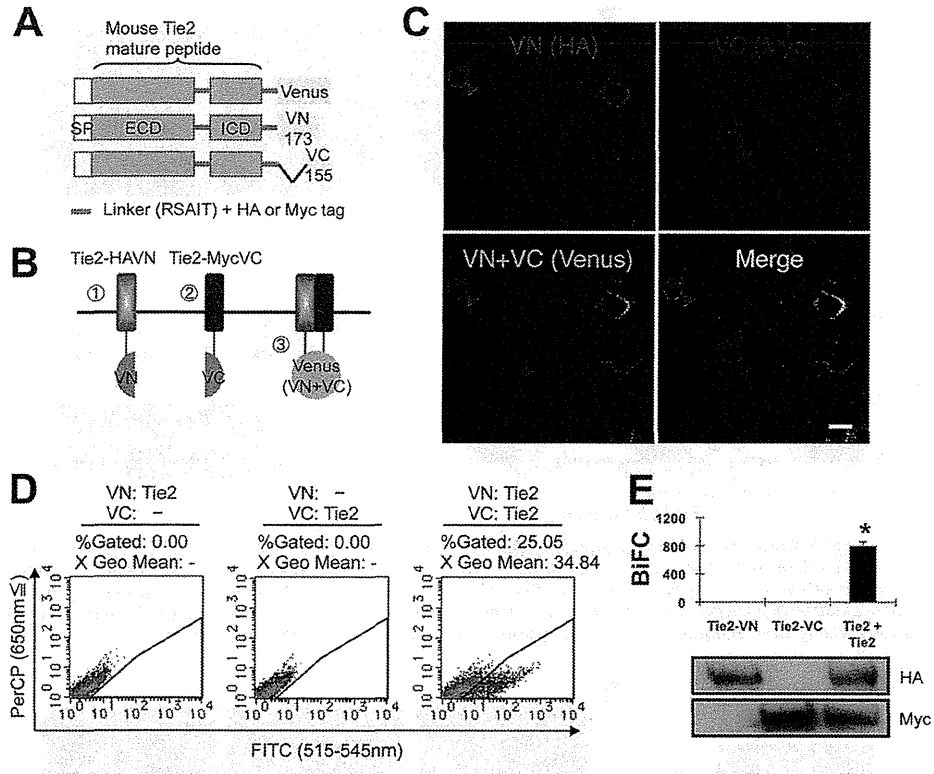

FIGURE 1. **BiFC analysis of Tie2 receptor homodimerization in living cells.** *A* and *B*, schematic representation of Tie2 tagged with either the N- or C-terminal of the Venus fragment (VN or VC). *SP*, signal peptide; *ECD*, extracellular domain; *ICD*, intracellular domain. When Tie2 dimerizes, fluorescence should reconstitute. *C*, HEK293T cells expressing Tie2-HAVN (*red*) and Tie2-MycVC (*blue*) observed by confocal microscopy. Cells were co-transefected with Tie2-HAVN and Tie2-MycVC expression vectors. Note that cells expressing Tie2-HAVN alone (*red arrowhead*) or Tie2-MycVC alone (*blue arrowhead*) develop no Venus fluorescence. *Bar* indicates 20 μm. *D*, flow cytometric analysis for evaluation of receptor dimerization as indicated. *E*, quantitative evaluation of Tie2 homodimerization in BiFC as observed in *D* (*, $p < 0.05$; $n = 3$). Protein expression level of each receptor was assessed by immunoblotting with anti-HA or anti-Myc Ab.

mouse anti-Myc Ab and Alexa Fluor 647 (blue)-conjugated anti-mouse Igs. BiFC fluorescence was detected using a filter for Alexa Fluor 488 (green). The slides were observed under a Leica TCS SP5 Ver1.6 (Leica Microsystems) using HCX PL APO lambda blue 63 × 1.4 oil. Images were processed using Adobe Photoshop CS5 Extended software (Adobe Systems).

Statistical Analysis—All data are displayed as the mean ± S.D. and were analyzed by two-tailed Student *t* test. A probability value of < 0.05 was considered statistically significant.

RESULTS

Establishment of Imaging Methods for Investigating the Dimerization of Tie2 Receptors—It has been reported that Tie2 is present in the form of dimers and/or oligomers on the cell surface (19). We also detected ligand-independent dimers of endogenous Tie2 in human umbilical vein endothelial cells (supplemental Fig. S1*A*). To assess Tie2 dimerization in the absence of Ang1, we utilized the BiFC assay (26). First, we prepared amino (N)-terminal (1–173: VN173) and carboxyl (C)-terminal (155–238: VC155) components of Venus fluorescent protein, a modifier of yellow fluorescent protein, fused with the C-terminal domain of wild-type (WT) mouse Tie2 with an HA or Myc tag linked to the molecule (Fig. 1*A*). When Tie2 (Tie2-HAVN, Tie2-MycVC) dimerizes, the fluorescent complex should be reconstituted (Fig. 1*B*). As expected, when Tie2-HAVN and Tie2-MycVC were cotransfected into HEK293T cells, cells expressing both HA and Myc developed fluorescence (Fig. 1*C*). Flow cytometry showed that transfection with both Tie2-HAVN and Tie2-MycVC vectors, but not with either alone, resulted in cells having high FITC intensity (Fig. 1, *D* and *E*). We confirmed that these co-transfectants developed BiFC fluorescence in cells expressing physiological levels of Tie2 as observed in ECs (supplemental Fig. S1, *B* and *C*).

Analysis of the Dimerization of Tie2-Tie1 using BiFC Assays—Ang1 activates Tie1 indirectly, mediated by its interaction with Tie2 (11, 12). It has been suggested that co-localization of Tie2 and Tie1 is induced upon activation of Tie2 by Ang1 (6). We investigated whether Tie2 and Tie1 also form heterodimers in a ligand-independent manner. Relative to Tie2, we found that the Tie1 protein was difficult to express in HEK293T cells following transfection of full-length Tie1 cDNA. However, when the original native signal sequence of Tie1 was excised and replaced with the Tie2 signal sequence (designated Tie1*), Tie1 expression was easily induced (Fig. 2*A*). Using this Tie1* construct, we evaluated Tie2-Tie1 and Tie1-Tie1 associations by BiFC. Although it has recently been reported that Tie2 and Tie1 associate following Ang1 stimulation and on cell-cell contact, we failed to detect any Tie2-Tie1 or Tie1-Tie1 associations (Fig. 2, *B–D*). This suggests that a Tie2 and Tie1 interaction is required for Ang1 binding to Tie2 and Tie1 and that Tie1 never gives rise to inactive dimers and/or oligomers in the absence of Ang1.

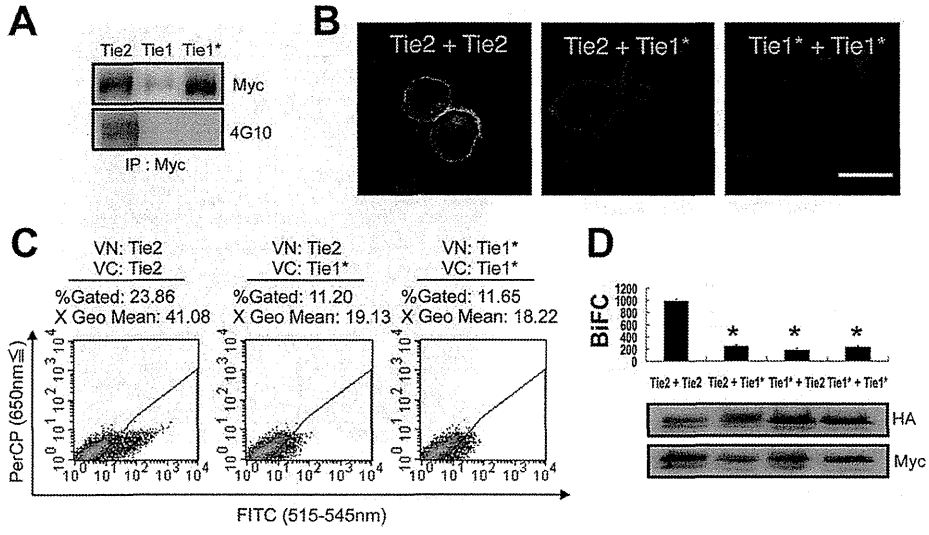

FIGURE 2. **BiFC analysis comparing Tie2 and Tie1*.** *A*, signal peptide of Tie1 was replaced with that of Tie2 (Tie1*). All receptors were C-terminally tagged with Myc. The levels of Tie2, Tie1, and Tie1* protein were analyzed with Myc or 4G10 Ab. *B–D*, HEK293T cells were transiently transfected in combination with Tie2-HAVN and Tie2-MycVC, Tie2-HAVN and Tie1*-MycVC, or Tie1*-HAVN and Tie1*-MycVC. *B*, cells were analyzed by confocal microscopy. *Bar* indicates 20 μm. *C*, flow cytometric analysis for evaluation of receptor dimerization as indicated. *D*, quantitative evaluation of receptor dimerization in BiFC as shown in *C* (*, $p < 0.05$; $n = 3$). Protein expression level of each receptor was assessed by immunoblotting with anti-HA or anti-Myc Ab.

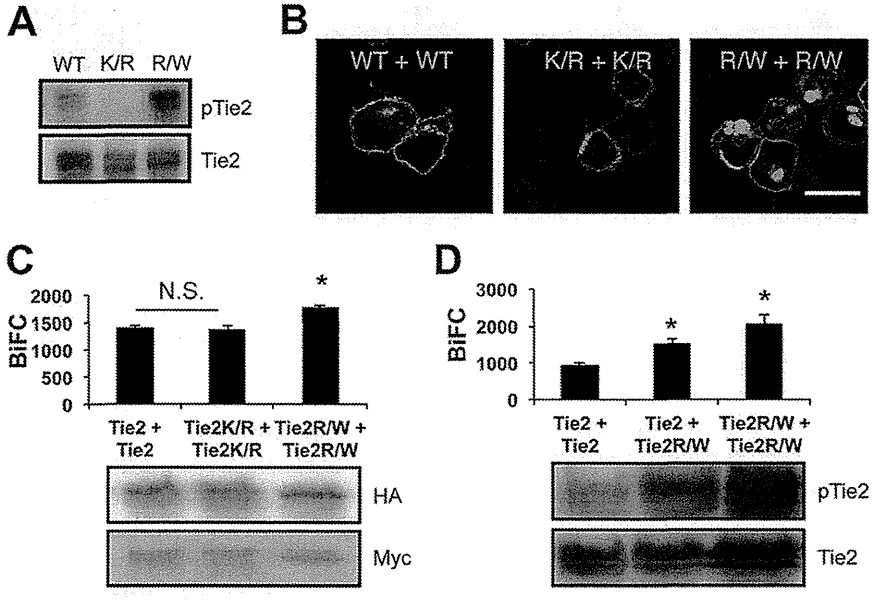

FIGURE 3. **BiFC analysis comparing Tie2 and Tie2 mutant.** *A*, detection of Tie2, kinase-dead mutant Tie2K854R (*K/R*) and constitutively active mutant Tie2R848W (*R/W*) phosphorylation. *B* and *C*, HEK293T cells were transiently transfected in combination with Tie2-HAVN and Tie2-MycVC, Tie2K854R-HAVN and Tie2K854R-MycVC, or Tie2R848W-HAVN and Tie2R848W-MycVC. *B*, cells were analyzed by confocal microscopy. *Bar* indicates 20 μm. *C*, quantitative evaluation of receptor dimerization in BiFC as shown in *B* (*, $p < 0.05$; $n = 3$). Protein expression level of each receptor was assessed by immunoblotting with anti-HA or anti-Myc Ab. *D*, quantitative evaluation of receptor dimerization in BiFC of Tie2 and Tie2R848W (*, $p < 0.05$; $n = 3$). Protein expression level of each receptor was assessed by immunoblotting with anti-Tie2. *N.S.*, not significant.

Analysis of the Dimerization of Tie2 Mutants Using BiFC Assays—Phosphorylation of overexpressed Tie1 and Tie2 was observed, but only Tie2 and not Tie1 was autophosphorylated in the absence of Ang1 stimulation (Fig. 2*A*). To test whether phosphorylation of Tie2 affects Tie2-Tie2 dimerization, we generated a kinase-inactive Tie2 mutant (Tie2K854R) (Fig. 3*A*). However, loss of phosphorylation did not affect Tie2 dimerization (Fig. 3, *B* and *C*, and supplemental Fig. S2A). We further confirmed that it was not until Ang1 bound Tie2 that dimerized Tie2 was internalized (supplemental Fig. S2*B*). Although dimerized WT Tie2 was observed in the cytoplasm, dimerized kinase-inactivated Tie2 did not internalize from the cell surface into the cytoplasm (Fig. 3*B*). Next, we constructed a constitutively active mutant of Tie2 (Tie2R848W) (Fig. 3*A*) (29). In HEK293T cells overexpressing Tie2R848W-HAVN and Tie2R848W-MycVC, more abundant Venus fluorescence was observed in the cytoplasm than in wt Tie2 or Tie2K854R (Fig. 3, *B* and *C*). Interestingly, Tie2R848W can dimerize with WT Tie2, resulting in BiFC intensity enhanced compared with Tie2-Tie2 dimers (Fig. 3*D*). These results suggest that our BiFC

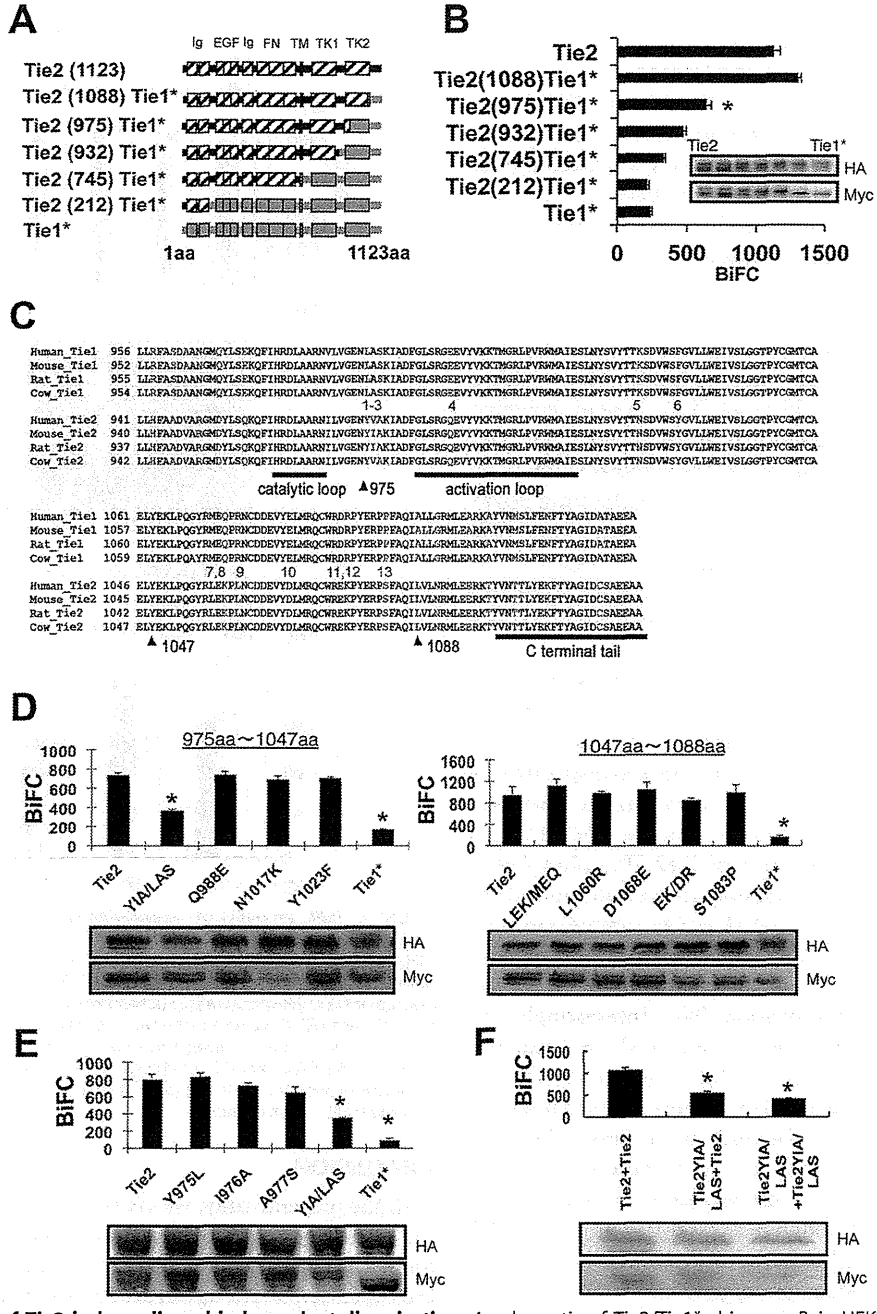

FIGURE 4. **YIA sequence of Tie2 induces ligand-independent dimerization.** *A*, schematic of Tie2/Tie1* chimeras. *B*, in HEK293T cells, Tie2-HAVN was transiently transfected in combination with Tie2, Tie2(1088)Tie1*, Tie2(975)Tie1*, Tie2(932)Tie1*, Tie2(745)Tie1*, Tie2(212)Tie1*, or Tie1* C-terminally fused with MycVC, and close associations of receptors assessed by BiFC and flow cytometry (*, $p < 0.05$; $n = 3$). The protein expression level of each receptor was confirmed by immunoblotting with anti-HA or anti-Myc Ab (*inset*). *C*, comparison of amino acid sequences of Tie1 and Tie2 C terminus from different species. *Pink*, different amino acids; *blue*, same amino acids (*aa*). *D* and *E*, in HEK293T cells, Tie2-HAVN was transiently transfected in combination with Tie2, Tie2YIA/LAS, Tie2Q988E, Tie2N1017K, Tie2Y1023F, Tie2LEK/MEQ, Tie2L1060R, Tie2D1068E, Tie2EK/DR, Tie2S1083P, or Tie1* C-terminally fused with MycVC (*D*) or Tie2, Tie2Y975L, Tie2I976A, Tie2A977S, Tie2YIA/LAS, or Tie1* C-terminally fused with MycVC (*E*), and close associations of receptors assessed by BiFC and flow cytometry. Protein expression level of each receptor was confirmed by immunoblotting with anti-HA or anti-Myc Ab (*inset*) (*, $p < 0.05$; $n = 3$). *F*, YIA domain of Tie2 was replaced by LAS sequence (Tie2YIA/LAS). Association of Tie2-Tie2, Tie2-Tie2YIA/LAS, and Tie2YIA/LAS-Tie2YIA/LAS was observed by BiFC as described above. Protein expression level of each receptor was confirmed by immunoblotting with anti-HA or anti-Myc Ab (*inset*) (*, $p < 0.05$; $n = 3$).

system mimics canonical receptor down-modulation only after activation of the receptor.

Identification of the Domain That Induces Ligand-independent Tie2 Homodimerization—We found that Tie2, but not Tie1, forms homodimers in a ligand-independent manner. Hence, we attempted to isolate the Tie2 ligand-independent dimerizing region. First, we sought domains responsible for Tie2-Tie2 association by replacing part of Tie2 with the Tie1 homologous domain (Fig. 4*A*). We found that lack of the extracellular domain of Tie2 did not affect BiFC (supplemental Fig. S3), suggesting that BiFC caused by Tie2-Tie2 interaction is mainly induced by the intracellular domain of Tie2 in our

model. Therefore, we focused on the intracellular domain of Tie2 for dimerization in our next experiments.

We transfected Tie2-HAVN and Tie2/Tie1* chimeric genes fused with Myc-tagged VC155 into HEK293T cells. When the C-terminal of Tie2 (from 975 to 1088 amino acids) was replaced by the Tie1 sequence, BiFC was significantly attenuated (Fig. 4*B*). There are differences in 13 amino acids between Tie2 and Tie1 (Fig. 4*C*). Therefore, we mutated Tie2 where its sequence is different from Tie1 domain by domain and observed Tie2-Tie2/mutant dimerization. We found that a YIA sequence within Tie2 (975–977) is critical for dimerization (Fig. 4*D*). Next, we introduced point mutations into this YIA domain. We found that no single mutation was responsible for reducing Tie2 dimerization, but rather the whole YIA tandem sequence was involved (Fig. 4*E*). We generated mutant Tie2 (Tie2YIA/LAS) in which the YIA domain of Tie2 was replaced by LAS. Tie2-Tie2YIA/LAS and Tie2YIA/LAS-Tie2YIA/LAS dimerization was not significantly different, suggesting that both Tie2 YIA domains in the cytoplasmic region are required for dimerization (Fig. 4*F*). When phosphorylation of Tie2YIA/LAS was assessed, it was found that mere overexpression did not induce it (supplemental Fig. S4).

Tie2YIA/LAS Monomer Mutants Can Be Dimerized and Phosphorylated by Ligand Binding—Tie2 can form ligand-independent inactive dimers; it has therefore been suggested that receptor dimerization and activation are mechanistically distinct and separable events (19, 30). Next, we analyzed whether Angl binding to the inactive monomer mutant Tie2YIA/LAS induced dimerization and activation of Tie2. Phosphorylation of WT Tie2 by exogenous Angl did not increase the intensity of BiFC developed by either Tie2-Tie2 (Fig. 5*A*). On the contrary, Angl stimulation decreased BiFC intensity after 30 min. This suggests that internalization and degradation of Tie2 was induced after Tie2 phosphorylation (30). Interestingly, we found that Tie2YIA/LAS prominently enhanced BiFC intensity under Angl stimulation for 1 h (Fig. 5*B*). Microscopy showed that Tie2 formed ligand-independent dimers and was internalized upon Angl stimulation (Fig. 6*A*). In contrast, Tie2YIA/LAS dimerization was not detected in the absence of Angl. However, BiFC signals due to dimerization did occur upon stimulation with Angl, although to a lesser extent than in WT Tie2. This suggests that YIA mutations in Tie2 did not completely prevent Tie2 dimerization (Fig. 6*B*).

Finally, we investigated how the lack of Tie2 ligand-independent dimerization affected its phosphorylation and downstream Erk signaling. When the time course of Tie2 phosphorylation was recorded in the presence of a fixed dose of Angl (200 ng/ml), no significant differences between wild-type Tie2 and Tie2YIA/LAS were observed (Fig. 7*A*). However, when phosphorylation was measured after stimulation for 10 min with different doses of Angl, Tie2 and Erk phosphorylation by Tie2YIA/LAS decreased at a high dose (350~500 ng/ml) of Angl compared with wild-type Tie2 (Fig. 7, *B* and *C*). These findings suggest that the YIA domain of Tie2 is not indispensable for dimerization of Tie2 but is used for forming non-ligand-mediated dimerization of Tie2 to effectively react to a higher dose of Angl.

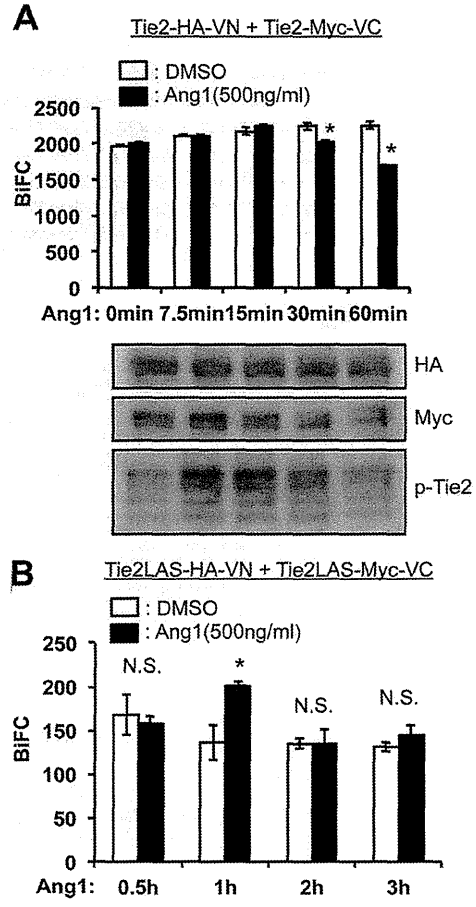

FIGURE 5. **BiFC analysis of ligand-dependent dimerization of Tie2.** *A*, dimerization of Tie2 was observed in Tie2-VN- and Tie2-VC-coexpressing NIH3T3 cells in the presence or absence of Angl stimulation. At each time point, cell lysates were analyzed for Tie2-HAVN and Tie2-MycVC as well as the degree of Tie2 phosphorylation (*lower panel*). Note that Angl stimulation did not enhance BiFC level but rather attenuated it 30 min after stimulation with Angl. *B*, time course of dimerization of Tie2YIA/LAS (Tie2LAS) was observed in Tie2 YIA/LAS-VN- and Tie2 YIA/LAS -VC-coexpressing HEK293T cells in the presence or absence of Angl stimulation (*, $p < 0.05$; $n = 3$). *DMSO*, dimethyl sulfoxide; *N.S.*, not significant.

DISCUSSION

In the present study, we visualized Tie2 dimerization by the BiFC method and sought ligand-independent dimerization domains of Tie2. A previous report showed that Tie2 clusters are expressed on the apical and basolateral plasma membranes (19). However, it was not clear whether Tie2 phosphorylation results in dimer formation. Here, we showed that kinase-inactive Tie2 mutants also form dimers in the absence of Angl. Thus, Tie2 can indeed form dimers without Angl. To analyze the role of ligand-independent dimerization of Tie2, a mutant that cannot form dimers in the absence of Angl is required. In the present study, we utilized a mutant with no evidence of Tie1-Tie1 dimerization even when overexpressed. Based on the amino acid sequence difference between Tie2 and Tie1, we found that YIA in the Tie2 cytoplasmic domain is important for ligand-independent Tie2 dimerization.

We show that the YIA domain required to form ligand-independent Tie2 dimers is situated between the catalytic and activation loops in the intracellular region of the molecule. Previ-

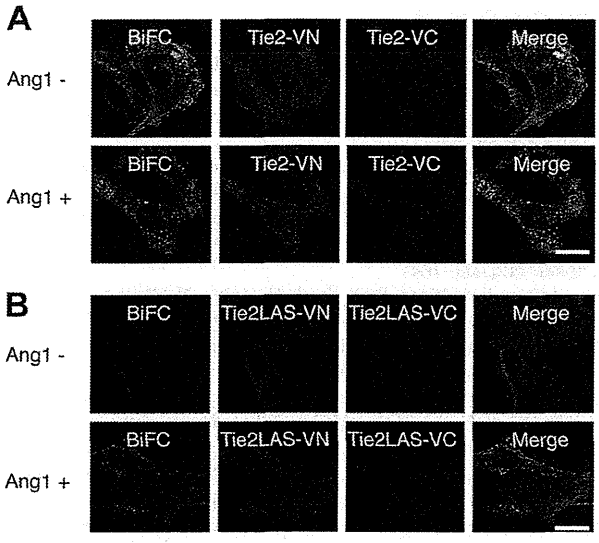

FIGURE 6. **Tie2YIA/LAS cannot form ligand-independent dimers but is dimerized and phosphorylated upon stimulation with Ang1.** *A*, dimerization and localization of Tie2 were observed in Tie2-VN- and Tie2-VC-coexpressing NIH3T3 cells in the presence or absence of Ang1. Wild-type Tie2 can form dimers irrespective of Ang1 stimulation, as confirmed by BiFC. However, this dimerized Tie2 forms cluster-like aggregations and is internalized upon stimulation with Ang1. *B*, similar to *A*, dimerization and localization of Tie2YIA/LAS (Tie2LAS) is observed in Tie2YIA/LAS-VN- and Tie2YIA/LAS-VC-coexpressing NIH3T3 cells. In the absence of Ang1, Tie2LAS did not dimerize but formed cluster-like aggregations upon stimulation with Ang1. *Bar* indicates 20 μm.

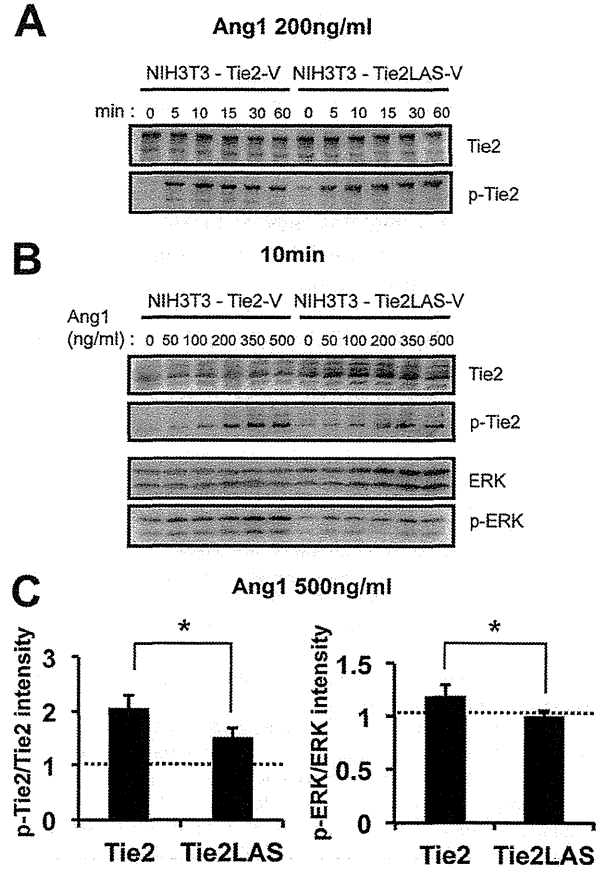

FIGURE 7. **Phosphorylation of Tie2 and Tie2 downstream molecule Erk.** *A*, Ang1 reactivity of Tie2 and Tie2YIA/LAS. After exposure to 200 ng/ml of Ang1, Tie2 and Tie2YIA/LAS phosphorylation was detected in a time-dependent fashion between 0 and 60 min. *B*, Ang1 reactivity of Tie2 and Tie2YIA/LAS. Ang1-mediated Tie2, Tie2YIA/LAS, and Erk phosphorylation was detected in a dose-dependent fashion between 0 and 500 ng/ml for 10 min. *C*, Tie2 and Erk phosphorylation on stimulation with 500 ng/ml Ang1 was quantified. The ratio of pTie2/Tie2 or pErk/Erk in cells on stimulation with Ang1 was compared with Ang1-untreated cells. (*, $p < 0.05$; $n = 3$).

ous reports show that the Tie2 C-terminal tail has a negative regulatory role in Tie2 signaling and function (31, 32). To activate Tie2, conformational changes in the intracellular loop structure and C-terminal tail are required for ATP and substrate binding. Therefore, it is possible that YIA domains control the movement of these loop and C-terminal tails. Further structural analysis of Tie2 will be necessary to assess how the YIA domain controls ligand-independent dimerization of Tie2 for folding and Tie2-Tie2 associations.

Unlike Tie2 homodimer formation, the BiFC method reveals that Tie2 and Tie1 scarcely interact. Recently, it has been reported that Tie2-Tie1 heterodimer formation is induced in the extracellular domain of Tie2 and Tie1, respectively, and that this occurs in the absence of angiopoietin ligation (33). Heterodimerization was observed using Tie receptors lacking intracellular domains. At present, it is difficult to explain this discrepancy, but it may simply be due to the absence of receptor cytoplasmic regions in the previous report. Indeed, when endogenous Tie2 and Tie1 localization in human umbilical vein endothelial cells was observed in the absence of Ang1, we found that Tie2 and Tie1 did not co-localize on the cell surface (supplemental Fig. S5). However, as previously reported, upon Ang1 stimulation, co-localization of these receptors does occur. In contrast, when NIH3T3 cells expressing Tie2-VN and Tie1*-VC were stimulated with Ang1, BiFC intensity was not enhanced (supplemental Fig. S6*A*). In addition, Ang1 activates both Tie2 and Tie1, but we did not observe a strong physical association between Tie2 and Tie1 in the immunoprecipitation analysis (supplemental Fig. S6, *B* and *C*). It has been reported that shedding of Tie1 extracellular domain itself induces Tie2 activation and that Ang2 acts as a Tie2 agonist upon Tie1 shedding (34–36). This suggests that Tie1 ectodomain shedding plays important roles in promoting Tie2 conformation changes and activation. Therefore, we cannot completely exclude the possibility that full-length Tie2 and Tie1 may heterodimerize under certain specific conditions in ECs.

It has been reported that Tie2 forms oligomers on the cell membrane (19); however, the function of such forms of Tie2 has not been elucidated. We found that a lack of ligand-independent dimerization of Tie2 led to attenuation of high dose Ang1-mediated activation of Tie2. This suggests that ligand-independent Tie2 dimerization plays a role in the rapid clustering of Tie2 upon activation with higher doses of Ang1 or in the preformation of Tie2 oligomers to respond to higher doses of Ang1. Further precise analysis of how ligand-independent dimerization of Tie2 relates to the extent of Tie2 phosphorylation at higher Ang1 doses is still required, including elucidation of the biological significance of Tie2 oligomers.

In humans, an amino acid substitution of tryptophan for arginine at residue (Tie2R849W) leads to ligand-independent constitutive activation; it is associated with familial venous malformations and causes thickness or lack of smooth muscle cells

in the veins systemically (14, 29, 37). In the present study, we showed that the intensity of BiFC signals from Tie2R848W-Tie2R848W was enhanced. Interestingly, Tie2R848W interactions with WT Tie2 were stronger than Tie2-Tie2 interactions. This suggests that Tie2R848W may heterodimerize with WT Tie2 and induce constitutive phosphorylation of WT Tie2. Therefore, analysis of regulatory mechanisms in ligand-independent dimerization domains may be useful for developing therapeutic strategies to inhibit Tie2 activation in patients suffering from venous malformation.

Acknowledgments—We thank T. Kamimoto, N. Fujimoto, and K. Fukuhara for technical assistance.

REFERENCES

1. Dejana, E., Tournier-Lasserve E., and Weinstein, B. M. (2009) The control of vascular integrity by endothelial cell junctions: molecular basis and pathological implications. *Dev. Cell* **16,** 209–221
2. Augustin, H. G., Koh, G. Y., Thurston, G., and Alitalo, K. (2009) Control of vascular morphogenesis and homeostasis through the angiopoietin-Tie system. *Nat. Rev. Mol. Cell Biol.* **10,** 165–177
3. Sato, T. N., Tozawa, Y., Deutsch, U., Wolburg-Buchholz, K., Fujiwara, Y., Gendron-Maguire, M., Gridley, T., Wolburg, H., Risau, W., and Qin, Y. (1995) Distinct roles of the receptor tyrosine kinases Tie-1 and Tie-2 in blood vessel formation. *Nature* **376,** 70–74
4. Davis, S., Aldrich, T. H., Jones, P. F., Acheson, A., Compton, D. L., Jain, V., Ryan, T. E., Bruno, J., Radziejewski, C., Maisonpierre, P. C., and Yancopoulos, G. D. (1996) Isolation of angiopoietin-1, a ligand for the TIE2 receptor, by secretion-trap expression cloning. *Cell* **87,** 1161–1169
5. Fukuhara, S., Sako, K., Minami, T., Noda, K., Kim, H. Z., Kodama, T., Shibuya, M., Takakura, N., Koh, G. Y., and Mochizuki, N. (2008) Differential function of Tie2 at cell-cell contacts and cell-substratum contacts regulated by angiopoietin-1. *Nat. Cell Biol.* **10,** 513–526
6. Saharinen, P., Eklund, L., Miettinen, J., Wirkkala, R., Anisimov, A., Winderlich, M., Nottebaum, A., Vestweber, D., Deutsch, U., Koh, G. Y., Olsen, B. R., and Alitalo, K. (2008) Angiopoietins assemble distinct Tie2 signalling complexes in endothelial cell-cell and cell-matrix contacts. *Nat. Cell Biol.* **10,** 527–537
7. Takakura, N., Watanabe, T., Suenobu, S., Yamada, Y., Noda, T., Ito, Y., Satake, M., and Suda, T. (2000) A role for hematopoietic stem cells in promoting angiogenesis. *Cell* **102,** 199–209
8. Dumont, D. J., Gradwohl, G., Fong, G. H., Puri, M. C., Gertsenstein, M., Auerbach, A., and Breitman, M. L. (1994) Dominant-negative and targeted null mutations in the endothelial receptor tyrosine kinase, tek, reveal a critical role in vasculogenesis of the embryo. *Genes Dev.* **8,** 1897–1909
9. Puri, M. C., Rossant, J., Alitalo, K., Bernstein, A., and Partanen, J. (1995) The receptor tyrosine kinase TIE is required for integrity and survival of vascular endothelial cells. *EMBO J.* **14,** 5884–5891
10. Puri, M. C., Partanen, J., Rossant, J., and Bernstein, A. (1999) Interaction of the TEK and TIE receptor tyrosine kinases during cardiovascular development. *Development* **126,** 4569–4580
11. Saharinen, P., Kerkelä, K., Ekman, N., Marron, M., Brindle, N., Lee, G. M., Augustin, H., Koh, G. Y., and Alitalo, K. (2005) Multiple angiopoietin recombinant proteins activate the Tie1 receptor tyrosine kinase and promote its interaction with Tie2. *J. Cell Biol.* **169,** 239–243
12. Yuan, H. T., Venkatesha, S., Chan, B., Deutsch, U., Mammoto, T., Sukhatme, V. P., Woolf, A. S., and Karumanchi, S. A. (2007) Activation of the orphan endothelial receptor Tie1 modifies Tie2-mediated intracellular signaling and cell survival. *FASEB J.* **21,** 3171–3183
13. Patan, S. (1998) TIE1 and TIE2 receptor tyrosine kinases inversely regulate embryonic angiogenesis by the mechanism of intussusceptive microvascular growth. *Microvasc. Res.* **56,** 1–21
14. Morris, P. N., Dunmore, B. J., Tadros, A., Marchuk, D. A., Darland, D. C., D'Amore, P. A., and Brindle, N. P. (2005) Functional analysis of a mutant form of the receptor tyrosine kinase Tie2 causing venous malformations. *J. Mol. Med.* **83,** 58–63
15. Maisonpierre, P. C., Suri, C., Jones, P. F., Bartunkova, S., Wiegand, S. J., Radziejewski, C., Compton, D., McClain, J., Aldrich, T. H., Papadopoulos, N., Daly, T. J., Davis, S., Sato, T. N., and Yancopoulos, G. D. (1997) Angiopoietin-2, a natural antagonist for Tie2 that disrupts *in vivo* angiogenesis. *Science* **277,** 55–60
16. Thomas, M., and Augustin, H. G. (2009) The role of the Angiopoietins in vascular morphogenesis. *Angiogenesis* **12,** 125–137
17. Eklund, L., and Olsen, B. R. (2006) Tie receptors and their angiopoietin ligands are context-dependent regulators of vascular remodeling. *Exp. Cell Res.* **312,** 630–641
18. Kim, I., Kim, J. H., Moon, S. O., Kwak, H. J., Kim, N. G., Koh, G. Y. (2000) Angiopoietin-2 at high concentration can enhance endothelial cell survival through the phosphatidylinositol 3′-kinase/Akt signal transduction pathway. *Oncogene* **19,** 4549–4552
19. Bogdanovic E., Coombs N., and Dumont D. J. (2009) Oligomerized Tie2 localizes to clathrin-coated pits in response to angiopoietin-1. *Histochem. Cell Biol.* **132,** 225–237
20. Jura, N., Endres, N. F., Engel, K., Deindl, S., Das, R., Lamers, M. H., Wemmer, D. E., Zhang, X., and Kuriyan, J. (2009) Mechanism for activation of the EGF receptor catalytic domain by the juxtamembrane segment. *Cell* **137,** 1293–1307
21. Red Brewer, M., Choi, S. H., Alvarado, D., Moravcevic, K., Pozzi, A., Lemmon, M. A., and Carpenter, G. (2009) The juxtamembrane region of the EGF receptor functions as an activation domain. *Mol. Cell* **34,** 641–651
22. Yu, X., Sharma, K. D., Takahashi, T., Iwamoto, R., and Mekada, E. (2002) Ligand-independent dimer formation of epidermal growth factor receptor (EGFR) is a step separable from ligand-induced EGFR signaling. *Mol. Biol. Cell* **13,** 2547–2557
23. Tao, R. H., and Maruyama, I. N. (2008) All EGF (ErbB) receptors have preformed homo- and heterodimeric structures in living cells. *J. Cell Sci.* **121,** 3207–3217
24. Livnah, O., Stura, E. A., Middleton, S. A., Johnson, D. L., Jolliffe, L. K., and Wilson, I. A. (1999) Crystallographic evidence for preformed dimers of erythropoietin receptor before ligand activation. *Science* **283,** 987–990
25. Chan, F. K., Chun, H. J., Zheng, L., Siegel, R. M., Bui, K. L., and Lenardo, M. J. (2000) A domain in TNF receptors that mediates ligand-independent receptor assembly and signaling. *Science* **288,** 2351–2354
26. Kerppola, T. K. (2006) Design and implementation of bimolecular fluorescence complementation (BiFC) assays for the visualization of protein interactions in living cells. *Nat. Protocols* **1,** 1278–1286
27. Morita, S., Kojima, T., and Kitamura, T. (2000) Plat-E: an efficient and stable system for transient packaging of retroviruses. *Gene Ther.* **7,** 1063–1066
28. Saitoh, T., Nakano, H., Yamamoto, N., and Yamaoka, S. (2002) Lymphotoxin-β receptor mediates NEMO-independent NF-κB activation. *FEBS Lett.* **532,** 45–51
29. Vikkula, M., Boon, L. M., Carraway, K. L., 3rd, Calvert, J. T., Diamonti, A. J., Goumnerov, B., Pasyk, K. A., Marchuk, D. A., Warman, M. L., Cantley, L. C., Mulliken, J. B., and Olsen, B. R. (1996) Vascular dysmorphogenesis caused by an activating mutation in the receptor tyrosine kinase TIE2. *Cell* **87,** 1181–1190
30. Bogdanovic, E., Nguyen, V. P., and Dumont, D. J. (2006) Activation of Tie2 by angiopoietin-1 and angiopoietin-2 results in their release and receptor internalization. *J. Cell Sci.* **119,** 3551–3560
31. Shewchuk, L. M., Hassell, A. M., Ellis, B., Holmes, W. D., Davis, R., Horne, E. L., Kadwell, S. H., McKee, D. D., and Moore, J. T. (2000) Structure of the Tie2 RTK domain: self-inhibition by the nucleotide binding loop, activation loop, and C-terminal tail. *Structure* **8,** 1105–1113
32. Niu, X. L., Peters, K. G., and Kontos, C. D. (2002) Deletion of the carboxyl terminus of Tie2 enhances kinase activity, signaling, and function. Evidence for an autoinhibitory mechanism. *J. Biol. Chem.* **277,** 31768–31773
33. Seegar, T. C., Eller, B., Tzvetkova-Robev, D., Kolev, M. V., Henderson, S. C., Nikolov, D. B., and Barton, W. A. (2010) Tie1-Tie2 interactions mediate functional differences between angiopoietin ligands. *Mol. Cell* **37,** 643–655
34. Yabkowitz, R., Meyer, S., Black, T., Elliott, G., Merewether, L. A., and Yamane, H. K. (1999) Inflammatory cytokines and vascular endothelial

growth factor stimulate the release of soluble tie receptor from human endothelial cells via metalloprotease activation. *Blood* **93,** 1969–1979

35. Marron, M. B., Singh, H., Tahir, T. A., Kavumkal, J., Kim, H. Z., Koh, G. Y., and Brindle, N. P. (2007) Regulated proteolytic processing of Tie1 modulates ligand responsiveness of the receptor-tyrosine kinase Tie2. *J. Biol. Chem.* **282,** 30509–30517
36. Singh, H., Milner, C. S., Aguilar Hernandez, M. M., Patel, N., and Brindle, N. P. (2009) Vascular endothelial growth factor activates the Tie family of receptor tyrosine kinases. *Cell Signal.* **21,** 1346–1350
37. Limaye, N., Wouters, V., Uebelhoer, M., Tuominen, M., Wirkkala, R., Mulliken, J. B., Eklund, L., Boon, L. M., and Vikkula, M. (2009) Somatic mutations in angiopoietin receptor gene TEK cause solitary and multiple sporadic venous malformations. *Nat. Genet.* **41,** 118–124

Identification of Vascular Endothelial Side Population Cells in the Choroidal Vessels and Their Potential Role in Age-Related Macular Degeneration

Taku Wakabayashi,[1,2] Hisamichi Naito,[1] Kazuhiro Takara,[1] Hiroyasu Kidoya,[1] Susumu Sakimoto,[1,2] Yusuke Oshima,[2] Kohji Nishida,[2] and Nobuyuki Takakura[1,3]

[1]Department of Signal Transduction, Research Institute for Microbial Diseases, Osaka University, Osaka, Japan
[2]Department of Ophthalmology, Osaka University Graduate School of Medicine, Osaka, Japan
[3]JST, CREST, Sanbancho, Chiyoda-ku, Tokyo, Japan

Correspondence: Nobuyuki Takakura, Department of Signal Transduction, Research Institute for Microbial Diseases, Osaka University, 3-1 Yamada-oka, Suita, Osaka 565-0871, Japan; ntakaku@biken.osaka-u.ac.jp.

Submitted: May 2, 2013
Accepted: August 31, 2013

Citation: Wakabayashi T, Naito H, Takara K, et al. Identification of vascular endothelial side population cells in the choroidal vessels and their potential role in age-related macular degeneration. *Invest Ophthalmol Vis Sci.* 2013;54:6686–6693. DOI: 10.1167/iovs.13-12342

Purpose. The neovascular form of age-related macular degeneration (AMD) is characterized by the growth of abnormal new blood vessels from the choroid, termed choroidal neovascularization (CNV). The origin of the new vessels in CNV, however, has not been elucidated fully to our knowledge. The purpose of this study is to identify vascular endothelial side population (SP) cells in the preexisting choroidal vessels, and investigate their potential role in AMD.

Methods. We made single cell suspensions of freshly isolated mouse choroidal, retinal, and brain tissue by enzymatic digestion. Vascular endothelial SP cells were isolated using flow cytometry based on the ability to efflux the DNA-binding dye, Hoechst 33342, via ATP-binding cassette (ABC) transporters.

Results. In the choroid, 2.8% of $CD31^+CD45^-$ vascular endothelial cells (ECs) showed a typical SP staining pattern. They were not bone marrow–derived and possessed high colony-forming capacity in vitro. They proliferated during laser-induced CNV in vivo. In contrast, stereotypic SP staining pattern was not observed in retinal and brain ECs. Retinal and brain EC-SP cells included increased SP populations with less colony-forming capacity within the SP compartment, because they contained cells with and without proliferative potential. The latter still could efflux the dye due to high levels of ABC transporters, such as ABCB1a, ABCC4, and ABCC6.

Conclusions. The EC-SP cells in the choroid may represent vessel-residing endothelial stem/progenitor cells contributing mainly to angiogenesis, and may be useful for augmenting vascular regeneration or for developing new antiangiogenic therapy in AMD.

Keywords: angiogenesis, endothelial cell, stem cell, side population, choroid

Ocular neovascular diseases, including diabetic retinopathy and the neovascular form of age-related macular degeneration (AMD), are the most common cause of severe vision loss worldwide.[1–3] Diabetic retinopathy is characterized by retinal ischemia accompanied by abnormal neovessel growth from the retinal vessels (retinal neovascularization),[1] whereas neovascular AMD is attributed to abnormal neovessel growth from the choroidal vessels (choroidal neovascularization [CNV]).[2,3] Retinal neovascularization and CNV are caused either by angiogenesis, a process involving new vascular endothelial cell (EC) sprouting from preexisting blood vessels,[4] or by vasculogenesis, involving bone marrow (BM)-derived circulating endothelial progenitor cells (EPCs) contributing to the neovasculature.[5–8] However, recent studies have suggested that the contribution of EPCs to neovessel formation is not as marked as reported previously.[9–12] Therefore, the main cellular origin of new ECs seems to be the vascular ECs residing in the preexisting blood vessels during angiogenesis-based neovessel formation.[11]

Vascular ECs residing in the preexisting blood vessels have been regarded as cells possessing equal potential to produce ECs in response to the angiogenic stimuli VEGF and bFGF. However, we recently identified a small population of vascular endothelial stem/progenitor cells in the preexisting blood vessels, which may be a source of new ECs during angiogenesis.[13] These cells were isolated using flow cytometry based on the side population (SP) phenotype, a common feature of adult stem cells, including hematopoietic, epidermal, and muscle stem cells characterized by the ability to efflux the DNA-binding fluorescent dye, Hoechst 33342, via ATP-binding cassette (ABC) transporters.[14–16] In contrast to the majority of cells that accumulate Hoechst 33342, termed main population (MP) cells, SP cells appear as a discrete unstained population to the side of the MP cells in a flow cytometry density dot plot. An SP cell population within the vascular ECs (EC-SPs) has been isolated from blood vessels in limb muscle.[13] Compared to non–EC-SP cells, EC-SP cells possess high proliferative potential in vivo and in vitro, consistent with their stem cell properties. However, EC-SPs in the retinal and choroidal vessels, and their role in angiogenesis have not been identified to our knowledge. In addition, EC-SP cells in the brain also have not been investigated in detail. In our study, we compared EC-SP cells in

the choroidal, retinal, and brain vessels to identify the origin of angiogenesis in those vessels.

Materials and Methods

Mice

The C57BL/6 mice and C57BL/6-Tg (CAG-EGFP) mice (EGFP mice) that express green fluorescent protein (GFP) in all tissues were purchased from Japan SLC (Shizuoka, Japan). Mice 8 to 12 weeks of age were used for experiments. All animal experiments were conducted in accordance with the ARVO Animal Statement for the Use of Animals in Ophthalmic and Vision Research.

Cell Preparation

Mice were euthanized and eyes were extracted. Retinal tissue was removed gently from the RPE-choroid-sclera complex. Choroidal tissue subsequently was scraped off the sclera. The whole brain also was extracted from the same mice. Respective tissue was excised, minced, and digested with Dispase II (Godo Shusei Corp., Chiba, Japan), collagenase (Wako, Osaka, Japan), and type II collagenase (Worthington Biochemical Corp., Lakewood, NJ) at 37°C.[17] The digested tissue was passed through 40-μm filters to yield single cell suspensions. Erythrocytes were lysed with ACK buffer (0.15 M NH_4Cl, 10 mM $KHCO_3$, and 0.1 mM Na_2-EDTA).

Flow Cytometry

Hoechst staining was performed as described previously.[14] Briefly, cell surface antigen staining was performed, and cell suspensions were incubated with Hoechst 33342 (5 μg/mL; Sigma, St. Louis, MO) at 37°C for 90 minutes in Dulbecco's modified Eagle's medium (DMEM, 2% fetal calf serum, 1 mM HEPES; Sigma) at a concentration of 10^6 nucleated cells/mL in the presence or absence of verapamil (50 μmol/L; Sigma). Cell surface antigen staining was performed as described previously.[18] The monoclonal antibodies (mAbs) used in immunofluorescence staining were anti-CD45 and anti-CD31 mAbs (eBiosciences, San Diego, CA). Respective isotype controls (eBiosciences) were used as negative controls. Propidium iodide (PI, 2 μg/mL; Sigma) was added before fluorescence-activated cell sorting (FACS) analysis to exclude dead cells. The stained cells were analyzed and sorted by a SORP FACSAria (BD Biosciences, San Diego, CA), and data were analyzed using FlowJo Software (Treestar Software, San Carlos, CA).

EC Colony-Forming Assay

The 10^3 EC-SP or MP cells were seeded on 24-well plates and cocultured on OP9 stromal cells in RPMI (Sigma), supplemented with 10% fetal calf serum (FCS) and 10^{-5}M 2-ME (Gibco, Grand Island, NY).[19] Cells were cultured for 10 days and the number of colonies counted after immunostaining.

Immunofluorescence

The procedure for staining was as reported previously.[20] For immunofluorescence, anti-CD31 mAb (BD Biosciences) was used for staining, and anti-rat IgG Alexa Fluor 488 (Invitrogen, Carlsbad, CA) and biotin-conjugated polyclonal anti-rat Ig (Dako, Glostrup, Denmark) were used as the secondary antibodies. Biotinylated secondary antibodies were developed using ABC kits (Vector Laboratories, Burlingame, CA). Cell nuclei were visualized with Hoechst dye (Sigma). Samples were visualized using an Olympus IX-70 equipped with UPlanFI ×4/0.13 and LCPlanFI ×20/0.04 dry objectives (Olympus Corporation, Tokyo, Japan). Images were acquired and processed with Adobe Photoshop CS3 software (Adobe Systems, Inc., San Jose, CA). All images shown are representative of more than four independent experiments.

Quantitative RT-PCR (qRT-PCR)

RNA was extracted from $CD31^+CD45^-$ EC cells, $CD31^+CD45^-$ EC-SP cells, and $CD31^+CD45^-$ EC-MP cells from the brain, retina, and choroid, respectively, using an RNeasy Mini Kit (Qiagen, Hilden, Germany), and cDNA was generated using reverse transcriptase from the ExScript RT reagent Kit (Takara, Otsu, Japan) as described previously.[21] Real-time PCR was performed using a Stratagene Mx3000P (Stratagene, La Jolla, CA). The polymerase chain reaction was performed on cDNA using specific primers (Supplementary Table S1). Expression level of the target gene was normalized to the GAPDH level in each sample.

Laser-Induced CNV

The C57BL/6 mice were anesthetized as described previously.[22] A total of 20 photocoagulation lesions was made with a diode laser (150 mW, 0.05 seconds, 75 μm; Ultima 2000 SE; Lumenis, Santa Clara, CA) between the retinal vessels in a peripapillary distribution in each fundus. Production of a subretinal bubble at the time of laser treatment confirmed the disruption of Bruch's membrane. The $CD31^+CD45^-$ ECs from the choroid were obtained 6 days after the laser procedure. Proportions and numbers of EC-SP cells per choroid were analyzed and calculated. Controls were the choroid from the untreated eye, or choroid from normal wild-type mice.

Murine BM Transplantation Model

The 8- to 12-week-old C57BL/6 mice underwent BM transplantation from same-aged EGFP donors. Briefly, BM cells were obtained by flushing the tibias and femurs of age-matched donor EGFP mice. The transplantation was performed into C57BL/6 mice lethally irradiated with 10.0 Gy, by intravenous infusion of approximately 1×10^7 donor whole BM cells. At 24 weeks after transplantation, by which time BM of recipient mice was reconstituted, the mice were used for the experiments. The percent reconstitution of the BM was confirmed in all mice at the time of experiments.

Statistical Analysis

All data are presented as mean ± SEM. For statistical analysis, SigmaStat software (SPSS, Inc., Chicago, IL) was used. When two groups were compared, a 2-sided Student's *t*-test was used. A probability value of less than 0.05 was considered statistically significant.

Results

Identification of Endothelial SP Cells in the Choroid, Retina, and Brain

We performed Hoechst 33342 staining and flow cytometric analysis of cells isolated from normal mouse choroid, retina, and brain to identify EC-SP cells. In the choroid, among cells positive for the EC marker CD31 and negative for the hematopoietic cell (HC) marker CD45 ($CD31^+CD45^-$ ECs, Fig. 1A), 2.8 ± 0.14% showed a typical SP staining pattern (i.e., Hoechst 33342 dye efflux properties, lost in the presence of the drug efflux pump inhibitor, verapamil, Fig. 1B). They were

Investigative Ophthalmology & Visual Science